

## TOPICAL REVIEW

# Density limits in toroidal plasmas

**Martin Greenwald**

MIT-Plasma Science &amp; Fusion Center, 175 Albany Street, Cambridge, MA02139, USA

Received 2 January 2002

Published 22 July 2002

Online at [stacks.iop.org/PPCF/44/R27](http://stacks.iop.org/PPCF/44/R27)**Abstract**

In addition to the operational limits imposed by MHD stability on plasma current and pressure, an independent limit on plasma density is observed in confined toroidal plasmas. This review attempts to summarize recent work on the phenomenology and physics of the density limit. Perhaps the most surprising result is that all of the toroidal confinement devices considered operate in similar ranges of (suitably normalized) densities. The empirical scalings derived independently for tokamaks and reversed-field pinches are essentially identical, while stellarators appear to operate at somewhat higher densities with a different scaling. Dedicated density limit experiments have not been carried out for spheromaks and field-reversed configurations, however, 'optimized' discharges in these devices are also well characterized by the same empirical law. In tokamaks, where the most extensive studies have been conducted, there is strong evidence linking the limit to physics near the plasma boundary: thus, it is possible to extend the operational range for line-averaged density by operating with peaked density profiles. Additional particles in the plasma core apparently have no effect on density limit physics. While there is no widely accepted, first principles model for the density limit, research in this area has focussed on mechanisms which lead to strong edge cooling. Theoretical work has concentrated on the consequences of increased impurity radiation which may dominate power balance at high densities and low temperatures. These theories are not entirely satisfactory as they require assumptions about edge transport and make predictions for power and impurity scaling that may not be consistent with experimental results. A separate thread of research looks for the cause in collisionality enhanced turbulent transport. While there is experimental and theoretical support for this approach, understanding of the underlying mechanisms is only at a rudimentary stage and no predictive capability is yet available.

**1. Introduction***1.1. Motivation*

Magnetic confinement experiments cannot operate over an arbitrary range of plasma densities. In addition to the operational limits imposed by MHD stability on plasma current and pressure,

an apparently independent limit on plasma density is observed. Even after extensive running time and sophisticated wall conditioning, each machine typically finds lower and upper density limits. The upper density limit is more important to the goal of practical fusion power since the fusion reaction rate scales with  $n^2$ . At constant pressure, the fusion reaction is maximized at an optimum temperature of the order of 10 keV, so plasma pressure cannot be arbitrarily partitioned between density and temperature. Reactor design studies typically find that densities of the order of  $10^{20} \text{ m}^{-3}$  are required [1]. The density at the optimum temperature can be computed as follows [2]:

$$\beta \propto \frac{n_{\text{optimum}} T_{\text{optimum}}}{B_{\text{T}}^2} \quad (1.1)$$

then, using standard definitions  $\beta_{\text{N}} \equiv (a B_{\text{T}} / I_{\text{P}}) \beta$  where  $I_{\text{P}}$  is in MA,  $B_{\text{T}}$  is in T, and  $a$  is in m.

$$n_{\text{optimum}} \propto \frac{\beta_{\text{N}} I_{\text{P}} B_{\text{T}}}{a} \quad (1.2)$$

using the most common empirical scaling for the density limit [3],

$$n_{\text{G}} = \frac{I_{\text{P}}}{\pi a^2} \quad (1.3)$$

where  $n_{\text{G}}$  is the line-averaged density in units of  $10^{20} \text{ m}^{-3}$ . It is found that

$$\frac{n_{\text{optimum}}}{n_{\text{G}}} \propto \beta_{\text{N}} a B_{\text{T}} \quad (1.4)$$

The design for international thermonuclear experimental reactor (ITER) was constrained by the need to operate at these high densities with a prediction of the density limit stated as one of its most critical needs [4]. For the ITER EDA, equation (1.4) yields  $n_{\text{optimum}}$  that exceeds  $n_{\text{G}}$  by 70%. The reference discharge for the newer ITER-FEAT design is optimized for  $n/n_{\text{G}} \sim 0.9$  [5]. Note that a reactor may still ignite even at a sub-optimum density, it simply is not achieving the maximum possible fusion yield at a given plasma pressure. The accessible density range affects other aspects of machine operation as well. In tokamaks, a transition from H to L-mode occurs as the limit is approached and disruptions are more frequent when running near the limit. Plasma purity and radiated power levels are typically strong functions of the density as are fuelling and pumping efficiencies, the performance of divertors (particularly, their ability to dissipate heat effectively) and the efficiency of current drive schemes.

Density limit experiments have two principal goals. The first is to find operational scenarios which maximize the density, particularly the central density, and second, to investigate the physics which underlies the limit. Techniques for wall conditioning [6–15] have been developed which enable operation at higher densities and methods such as central fuelling or edge pumping, which can lead to peaked density profiles, and have allowed operation at higher average and peak density as described below in sections 2.2.3 and 2.2.6. Understanding the mechanism for the density limit is crucial for extrapolating machine performance into untested regimes. For example, if the density limit were determined entirely by global power balance between input power and radiation, a fusion device might be able to run at arbitrarily high densities since both fusion heating power and radiation losses would increase with  $n^2$  [16]. On the other hand, there is a substantial body of evidence which suggests that a limit exists which is largely independent of the input or radiated power. While empirical scaling laws have done a reasonable job in describing data from many recent experiments, they can only hint at the underlying physics. It seems likely that robust, reliable predictions will only come from the development of a first-principles theory for the density limit backed up by detailed experimental observations. The extensive work already accomplished and reviewed here should provide a solid basis for such development.

## 1.2. Background

### 1.2.1. Early observations and empirical studies

Reports of a disruptive density limit date back to some of the earliest experiments on tokamaks carried out in the mid–late 1960s [17–19]. While the plasmas in these experiments were burdened with impurities and techniques for wall conditioning and fuelling were not well developed, many of the basic features of the limit were observed and catalogued. Strong MHD oscillations accompanied by shrinkage of the current channel, inferred from changes in plasma induction, were seen as the disruptive limit was approached. By the mid 1970s, enough data on this phenomenon had accumulated to begin scaling studies. Data from 13 circular, Ohmically heated machines with a wide range of operating parameters (maximum densities ranged from  $0.1 \times 10^{20}$  to  $3.5 \times 10^{20}$ ) were compiled and compared [20]. A scaling law was found where the maximum density,  $n_M = B_T/R$  with  $R$  the major radius in m. This relation, which became known as the ‘Murakami limit’ was interpreted as an expression of global power balance between neutral or radiation losses and the Ohmic input power which was roughly proportional to the central current density  $j_0 \sim B_T/R$ . Most of the data was for experiments with fill gas only and no puffing and yielded plasma densities which clustered at about 1/3 of the value predicted by later scalings. Results with gas puffing from Pulsator and Alcator showed densities about a factor of 2 higher. The DITE group plotted the operating space for their device by graphing plasma current vs density [21], later using a normalized form showing  $1/q$  vs  $n/n_M$  [22, 6]. This ‘Hugill’ plot showed the disruptive limit for high current (low  $q$ ) operation as well as the density limit and became a standard method of displaying the operating space for tokamaks as well as reversed-field pinches (RFPs). Figure 1 shows a rough schematic of the operating space for a tokamak and the various limits discussed in this section. As data were added to these plots, particularly from discharges with auxiliary heating, it became clear that there was an important relationship between the maximum attainable plasma density and the current density [23, 24]. Note that for circular, high aspect ratio plasmas,  $B_T/qR \sim I_p/a^2$ .

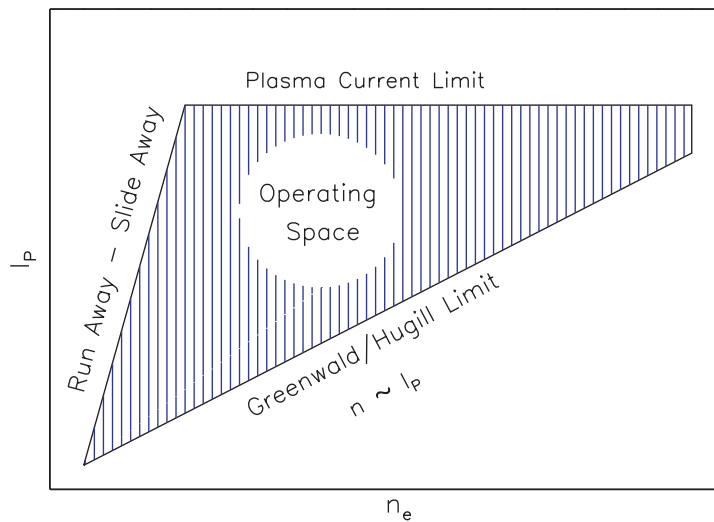


**Figure 1.** A schematic of the operating space for tokamaks or RFPs. Operation is bounded by a low-density limit characterized by run-away fast electrons and a high-density limit proportional to the plasma current. The limit on plasma current is due to MHD kink instabilities and applies to tokamaks.

Results with neutral beam injection (NBI) heating showed that this relationship did not depend in an important way on input power [25]. (This conclusion cannot be demonstrated with Ohmically heated experiments alone since the power and current are strongly covariant in this case.) This scaling, in the form  $n = B/qR$  came to be called the Hugill limit. It was also recognized that RFP devices showed a very similar density limit [26, 25]. In these devices, the operating range was parameterized as  $I/N$ , where  $I$  is the plasma current and  $N$  is the number of particles per unit toroidal length. Simple algebra shows that this is equivalent to  $n \propto I_p/a^2$  or  $B/qR$ .

During the next decade, as data from new experiments became available, quantitative discrepancies with the density limit scaling were found. That is, the coefficient in front of  $B/qR$  was found to vary from machine to machine. (This was not always readily apparent since different definitions for  $q$  were used in publications.) For a high aspect ratio circular device, the difference between the simplest analytic expressions for  $q$  in a straight cylinder wasn't much different than the MHD  $q$  derived from an equilibrium calculation. However, for strongly shaped plasmas the difference could be a factor of 2 or more. As part of the conceptual design for a burning plasma experiment, an effort to assess this problem was undertaken [3]. Figure 2 shows the boundaries in operating space in Hugill's space for the set of tokamaks used in this study. With  $1/q_\psi$  as the dependent parameter, no common limit was seen. The new scaling,  $n_G = I_p/\pi a^2$  was found which was equal to the Hugill limit for circular machines but which was substantially higher for experiments with shaped cross sections. Results of that scaling using the same data that went into figure 2, can be seen in figure 3. (Recent data from strongly shaped tokamaks, e.g. the spherical tokamak, MAST, demonstrate how important these shaping factors can become [27].) This limit is known as the Greenwald limit and is a common figure of merit for high-density operation. It has been written in the literature as  $n_G$ ,  $n_{GR}$ , or  $n_{GW}$ ; this review will use the former notation in equations and will also use it synonymously with 'empirical density limit'. The ratio  $n/n_G$  will be referred to as the 'normalized density'. In general, subsequent experiments have been in approximate agreement with this scaling and there has not been a renewed effort to assemble a multi-machine database and refine the fit. Discharge regimes which allow operation above the empirical limit have been the subject of intense investigation. Further information on these regimes and more detail on empirical scaling of the density limit can be found in section 2.

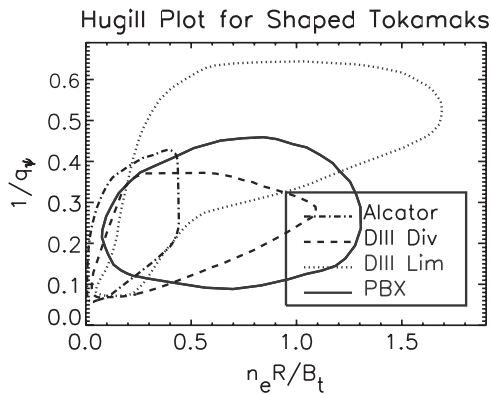


**Figure 2.** The operating boundaries plotted in Hugill's space for a set of tokamak data used for derivation of the Greenwald density limit. With  $1/q_\psi$  as the independent axis, no common limit was observed. The deviation was most marked for strongly shaped plasmas, PBX and DIII (diverted) [3].

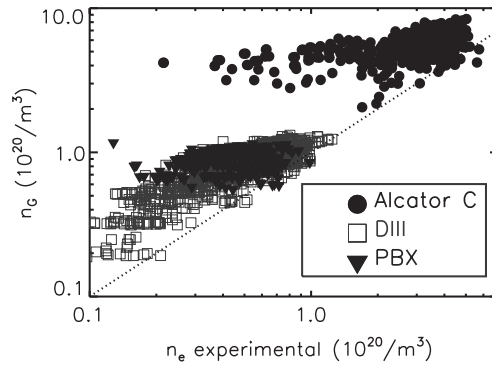


**Figure 3.** Measured densities are plotted against the Greenwald limit for the same set of data that was used in figure 2. Use of  $I_p/a^2$  instead of  $B/qR$  brought the circular and shaped plasmas into agreement [3].

### 1.2.2. Physics correlated with the density limit scaling

The density limit provides a rough normalization for many density-dependent phenomena, even when far from the disruptive limit. Plasma density would seem to be bounded by two limits, both of which are proportional to plasma current density. In the absence of field errors which can cause locked modes and reduce the accessible operational range, the low-density limit for tokamaks and RFPs sets in at about 5–10% of the high-density limit [28, 29]. This limit is often associated with slide-away or run-away regimes in which the drift parameter,  $v_{\text{drift}}/v_{\text{thermal}}$  is critical. Note that  $V_{\text{drift}} \propto J/n$ . As reported by Murakami, the ‘natural’ density for unfuelled Ohmic discharges turns out to be about  $0.3\text{--}0.4n_G$  [20]. The data in this reference included a scan from the ORMOK device which showed a linear dependence between the achieved density and the plasma current. Analysis of data from the international tokamak database has shown that the boundary between the linear and saturated confinement regimes scales like the density limit, occurring at about  $n/n_G \sim 0.4$  [30, 4]. The ‘natural’ density for ELMy H-modes (achieved when gas puffing is turned off at the L/H transition) also falls within a well defined range in density normalized to the density limit, typically 0.4–0.6 [31, 32]. With moderate gas puffing, JET reports  $n/n_G$  of 0.75 independent of heating method or power [33]. Overall, data residing in the international database for ELMy H-modes from 17 tokamaks have an average value of  $0.55n_G$  with a standard deviation of 0.2 [31]. In H-mode, the transition from type I to type III ELMs and the back transition to L-mode can both be characterized by  $n/n_G$  (for references and further details, see section 2.2.1.2). Studies of the scrape-off layer (SOL) plasma have found that temperature scale lengths and floating potential scale with  $n/I_p$  [34, 35]. In RFPs,  $I/N$  provides a good scaling parameter for  $Z_{\text{eff}}$  and  $\beta$  [36]. Finally, note that the critical  $\beta_N$  for the onset of tearing modes can be scaled with  $n/n_G$ . All of these results suggest that the density limit may not be simply due to critical phenomena which arise only near the limit, but rather is the result of gradual trends which hold across a broad range of densities.

### 1.3. Approach and organization

This review will attempt to survey recent work on the density limit with a particular emphasis on those studies which may shed light on the underlying physical mechanisms. Extension of

the empirical scaling to include recent data will not be attempted, though parameters which lead to significant deviations from the current scaling will be identified. Since the ultimate goal is to predict where in parameter space the density limit will occur, this physics will be stressed rather than the details of the limiting collapse. Thus, the MHD phenomenon observed during a density limit collapse will be discussed only briefly. The limit is apparently not extended by special attention to equilibrium, or MHD stability. While results from the widest possible range of toroidal confinement types will be presented, the balance of the published paper necessarily leads to more detail from tokamak experiments than from others. Section 2 describes experimental observations of the density limit for a variety of confinement experiments and device types. The importance of various parameters is discussed with emphasis on those which are not explicitly included in the empirical scalings. Section 3 summarizes various mechanisms proposed for the density limit including supporting and contradictory experimental data. A brief summary is outlined in section 4 followed by a discussion of the major issues and prospects for future work in section 5.

## 2. Observations and parametric dependence of density limits

### 2.1. Introduction

Investigations into operational limits must necessarily deal with certain complexities and ambiguities. The density limit is usually studied by vigorously fuelling a plasma and observing the effects. Researchers must assess the degree to which the effects observed are due to the intrinsic physics of the device or due to the techniques used for fuelling. Unfortunately, the plasma physics responsible for gas fuelling, the transport of particles up a density gradient from the edge to the core, is only poorly understood. Further, gas fuelling necessarily involves the complications of neutral interactions, wall recycling, atomic radiation and so forth. The relevant atomic processes are well understood but calculation of the rates requires detailed knowledge of edge profiles and the two- (or three-) dimensional distribution of neutrals. The role of fuelling from neutral beams is not much discussed in the literature, but can clearly play an important role. Researchers on many experiments have reported ‘fuelling limits’ where the ability to raise the density is attributed to a deficiency in the particle source rather than in the plasma response [37, 38, 8, 39–41, 32, 27]. In assessing density limits in general, one must also note that experiments typically do not achieve their highest densities until they reach a certain maturity—there is clearly a learning curve which must be traversed—and it would not be wise to place too much emphasis on the earliest data from a new machine.

The plasma response which defines the density limit, may be a degradation in temperature or confinement, a change of regimes, or a sudden termination of the discharge. Density limits in stellarators are apparently always of the first type, while RFPs and tokamaks manifest all three types of behaviour. Tokamaks in H-mode first show degraded confinement and a change in ELM activity [42] before making a transition to L-mode and finally disrupting. RFPs also show disruptive behaviour when the density is pushed at high density and current [13]. When data from different experiments are studied, one must be consistent about which density limit phenomena are being compared. Finally, the limit often manifests itself as a catastrophe—a disruption or a discontinuous change in regimes which is accompanied by nearly simultaneous changes in many observable parameters. Sorting out cause and effect in such a situation can be extremely difficult. Defining an operational boundary quantitatively presents its own difficulties. These issues will be addressed in section 2.2.2.

## 2.2. Tokamaks

Tokamaks confine plasma with poloidal fields which arise from currents driven in the plasma itself. Flux surface-averaged stability is provided by a strong toroidal field. The plasma is subject to large scale instabilities, driven by the plasma current and pressure, which can destroy the plasma if excited. Small scale instabilities are typically present and lead to significant particle and energy transport.

### 2.2.1. Plasma behaviour at high densities

**2.2.1.1. General observations.** As the density is raised toward the limit in a tokamak, a wide variety of phenomena is encountered in sequence. Summarized in table 1, these phenomena include the appearance of MARFEs, divertor detachment, a drop in H-mode confinement, changes in ELM activity, the H/L transition, poloidal detachment, current channel shrinkage, a rise in MHD activity, and finally major disruptions. Cooling of the plasma edge is a key element in all of them, reinforcing the importance of the edge plasma in the density limit that was suggested by early experiments [19, 22]. This notion has been more firmly established by studies of plasmas with peaked density profiles [43–51] as detailed in section 2.2.6 below. The effects listed are essentially universal with only the obvious exceptions—devices without divertors don't observe divertor detachment, experiments in L-mode won't see the H-mode effects, and so forth. The first four, MARFEs, divertor detachment, H-mode confinement degradation and the changes in ELM behaviour, can have their onset over a wide range of densities (from perhaps 0.3–0.9 $n_G$  depending on machine details) which are not entirely understood. The precise definitions of these phenomena and the densities at which they occur are crucial quantitative questions since their onset have been used as criteria for various theoretical calculations of the density limit. The last five, the H/L transition, poloidal detachment, shrinkage of the current channel, strong MHD activity and disruptions, tend to occur at or very near the limit. Of course, the H/L transition defines the H-mode density limit, and a disruption, by its nature, defines the overall limit.

The edge cooling which precedes density limiting phenomena is generally attributed to radiation. While the impurity content, as measured by  $Z_{\text{eff}}$ , usually drops with density [52],

**Table 1.** Phenomena which occur at high density and often associated with the density limit are shown along with the range of normalized densities at which they are observed.

| Phenomena                  | Range of normalized densities ( $n/n_{\text{limit}}$ ) | References   |
|----------------------------|--|--|
| MARFEs                     | 0.4–1  | [62, 64, 65, 219, 220, 34, 221, 66, 217, 222, 57, 37, 226, 71, 9, 227, 72, 224, 73, 39, 74, 225, 143, 46, 223] |
| Divertor detachment        | 0.3–1  | [75–81] [234, 235, 9, 72, 73, 88, 83, 82, 87, 236, 239, 86, 85, 84, 46, 237, 47, 238, 105, 223]                |
| Drop in H-mode confinement | 0.3–1  | [103, 89, 97, 90, 32, 91, 105, 102, 106, 50, 51]   |
| Change in ELM character    |  | [79, 42, 60, 90, 272, 32, 245, 91, 105]  |
| H/L transition             | 0.8–1  | [68, 89, 41, 85, 90, 92, 93, 32, 91]   |
| Poloidal detachment        | 0.7–1 (for clean plasmas)                              | [124, 67, 125, 222, 57, 8, 108, 53, 191]   |
| MHD and disruptions        | ~1   | [116, 110, 55, 56, 111, 112, 117, 113, 118, 114, 115, 123, 121, 119, 120, 122]                                 |

overall radiation, which scales as  $n_e n_Z$ , usually increases. Improvements in wall conditioning which leads to lower levels of impurities have also allowed operation at higher densities [22, 6–15] at least up to a point. It is notable however, that experiments where  $Z_{\text{eff}}$  is reduced below 2–2.5 don't see a further increase in the limit [3, 53]. Recent experiments have identified an increase in edge turbulence as the possible source for edge cooling at higher densities [54]. In some cases, most notably JET, the density limit is reported to correspond to  $P_{\text{rad}}/P_{\text{in}} \sim 1$  [55, 56]. Radiation is seen to increase nonlinearly with density, growing by about a factor of 2 in the last half second before the disruption during which time the density rises by no more than 5% [57]. This result is similar for discharges run in JET with both carbon and beryllium plasma facing components [58]. In the case of beryllium walls, the discharge does not proceed to a disruption but instead undergoes a series of relaxation oscillations driven by changes in radiated power, fuelling efficiency and density [59]. ASDEX has found much lower radiated power fractions at the density limit, in the range of 30–40% from the main chamber [8, 9] and not exceeding 60–70% when radiation from the divertor is included [7]. ASDEX Upgrade reports density limits with  $P_{\text{rad}}/P_{\text{in}}$  between 60% and 80% [60, 41]. These differences are perhaps due to different interpretations of the transient behaviour which occurs as a discharge proceeds to the limit. During this period, the radiation increases rapidly in a positive feedback loop with the rapidly dropping electron temperature. It is worth noting that the observation of density limiting disruptions with radiation at only a fraction of the input power has a long history. T3 reported an increase in  $P_{\text{rad}}/P_{\text{in}}$  with density reaching a maximum of about 30% as the disruptive limit was approached [61]. DITE reported the radiated fraction at about 50% at the limit. The role of radiation as a principal cause for the density limit, rather than as a correlation is discussed in detail in section 3.2.

**2.2.1.2. MARFES.** First reported on the Alcator C, ASDEX, Doublet III and FTU tokamaks, a MARFE is a toroidally symmetric, poloidally localized, strongly radiating region of high density and low temperature, typically seen on the high-field side of a tokamak [62–65, 34]. The original observations were on limited machines [66], however, similar phenomena have been observed on divertor experiments as well [67, 46, 47]. Divertor machines also exhibit what are sometimes called 'X-point MARFES' and 'divertor MARFES' which correspond to conduction-limited and detached operation, respectively, and are due to similar but not identical physics. Note that these terms do not have universally accepted definitions.

MARFES are a manifestation of a radiative collapse or 'condensation' which results from the local imbalance between input power and radiation. Over certain temperature ranges, partially ionized impurities radiate more power at lower temperatures; i.e.  $dP_{\text{rad}}/dT_e < 0$ . If conduction and convection are not able to supply enough power, the situation is unstable, with the temperature dropping and radiation further increasing. The requirement for pressure balance leads to a concomitant increase in local density, further accelerating the collapse. The temperature will continue to drop until  $dP_{\text{rad}}/dT_e$  becomes sufficiently less negative to bring the local plasma back into equilibrium, usually at temperatures less than 10 eV [66, 9]. Since atomic ionization and excitation increase as  $n_e n_Z$ , radiative collapses are more likely as the density is raised. The conditions for radiative instability occur at low temperature, radially localizing MARFES to the plasma periphery, typically to the SOL. As the density is raised, MARFES have been observed to expand radially inward toward the core plasma [68, 69, 46, 70].

In some cases, MARFES are seen just before the density limit is reached prompting theories of the density limit based on the stability condition for MARFE formation. ASDEX, ASDEX Upgrade, FT, JT-60, DIII-D, and JET have reported the appearance of MARFES at densities just below the disruptive limit [57, 71, 9, 72–74]. However, while the formation of MARFES is generally well parameterized by the density normalized to the density limit,  $n/n_G$ , many

experiments report MARFE formation at densities well below the limit. Machines as diverse as Alcator-C, C-Mod, Doublet III, DITE, and TFTR found MARFE thresholds in the range  $0.4\text{--}0.55n_G$  [66]. FTU has found that MARFEs form at a variable fraction of the density limit with dependences on input power,  $Z_{\text{eff}}$  and limiter material [39]. Experiments with beryllium first wall materials in JET found a MARFE formation density which scaled as  $P_{\text{in}}^{0.5}$  [37]. In part, the difference in these observations may be the result of differences in definitions or diagnostics. In some cases, MARFEs were seen to begin as highly localized structures which would not have been visible in machines without good diagnostic coverage. As the density was raised, the MARFEs expanded poloidally and radially, becoming more visible. In some cases, where the full dynamics are observed, authors have used the expansion of MARFEs as the cited precursor. The differences in diagnostics and interpretation do not seem to be sufficient, in all cases, to account for the different observations of the threshold which must instead, be due to some persistent but poorly understood physics.

*2.2.1.3. Divertor detachment.* At high density, conditions of low temperature and strong radiation occur in the divertor region as well. An ordered succession of regimes occurs as the power per particle is reduced. These operational regimes are defined in terms of the variation in plasma parameters along the open field lines from the midplane to the divertor strike point. At the lowest densities (and/or highest input powers) the plasma is in the ‘sheath limited’ regime where density temperature and pressure are constant. As the density is raised (and/or power lowered) the SOL plasma enters the ‘conduction limited’ regime in which the temperature drops near the divertor strike point. Momentum conservation requires constant pressure so the density near the strike point increases accordingly. At this point, a radiative collapse can occur leading to what some (but not all) authors term a ‘divertor MARFE’. At still higher densities (and/or low powers), collisions between plasma ions and neutrals become important providing a sink for momentum and leading to a drop in plasma pressure near the strike point. This condition is called ‘divertor detachment’ and is seen to occur when the electron temperature at the strike point drops to around 5 eV. Detachment can be seen in data from ASDEX as early as 1983 [75] but was not studied extensively until the early 1990s [75, 72, 76–81]. Detachment does not occur on all flux surfaces simultaneously, but begins near the separatrix and extends radially outward into the SOL as the density is raised [82, 46]. In the early stages of this process, usually termed ‘partial detachment’, the low temperature, strongly radiating region is tied to the strike point; however, as the detachment completes its radial extension, it jumps to the X-point. This phenomena is often called an ‘X-point MARFE’. The divertor often exhibits in–out asymmetries, with plasma parameters differing in the inner and outer divertor legs. These asymmetries can depend on the direction of the toroidal field, with higher densities on the inner divertor leg when the field is in the ‘normal’ configuration, i.e. with the  $\nabla B$  drift toward a single null divertor [83]. Detachment follows the asymmetry, occurring more readily on the inner divertor leg in this case.

Detachment tends to occur as the power per particle is reduced. Just as in the case with MARFEs, the detachment threshold does not occur at the same fixed fraction of the density limit on all machines. ASDEX [9] and JET [84] report complete detachment at densities just below the limit. In DIII-D, detachment is seen at  $0.6\text{--}0.7n_G$  [85], with some weak dependence on input power,  $n_{\text{detachment}} \sim P^{0.15}$ . Good H-mode confinement was maintained in this case, until the detachment completed and an X-point MARFE was formed. An increase in fuelling efficiency and impurity levels accompanied complete detachment [86, 47]. JT60-U saw detachment at similar densities, roughly  $0.7\text{--}0.75n_G$  but almost independent of power in this case. In its standard configuration, Alcator C-Mod, reported detachment in the range  $0.3\text{--}0.4n_G$  with a nearly linear dependence on input power [77]. However, divertor geometry was found to

have an important influence on the detachment threshold in C-Mod, with flat-plate divertor configurations detaching at densities 50–80% above the levels found for the standard inclined-plate geometry [87]. ASDEX Upgrade observed X-point MARFEs which existed stably at densities well below the limit ( $n_{\text{detachment}} \sim 0.5n_G$ ). The limit was associated instead with the movement and expansion of the MARFE. In this device, the threshold for X-point MARFE formation was linear with power [73], the plasma could always be made to detach if the power were low enough. ASDEX Upgrade also reported the ‘completely detached H-mode’ (CDH) regime which began at about  $0.65n_G$  [88]. The MARFEs were less stable for plasmas with the  $\nabla B$  drift away from a single null divertor and disrupted at densities at only 60–70% of those with the ‘normal’ field direction. This difference was attributed to an increase in impurity fluxes for the ‘reversed’ field case.

**2.2.1.4. Effects on H-mode confinement and character:** Density limit disruptions do not occur directly from H-mode plasmas. As the density is raised toward the limit, confinement usually degrades accompanied by a change in ELM character, followed by a transition to L-mode. These phenomena are extremely important as fusion reactors based on the H-mode regime require both high density and good confinement. Discharges with peaked density profiles can compensate to some extent by increasing the peak density relative to the average and by improvements in core confinement which are correlated with peaked density or pressure profiles. These effects are discussed in greater detail in section 2.2.6. The H/L transition occurs quite close to the disruptive limit in all machines and for standard H-modes with flat density profiles, the transition is reasonably well characterized by the Greenwald scaling. ASDEX Upgrade, C-Mod, DIII-D, JET, and JT60-U report an ‘H-mode’ limit at 0.9, 0.8, 0.85, 0.95, and  $1n_G$ , respectively [89, 85, 90, 32, 91]. The relation between the H/L and disruptive limits can be seen clearly when the threshold power is plotted against the normalized density as in figure 4 [68, 41, 92, 93]. The required power increases dramatically as the density limit is

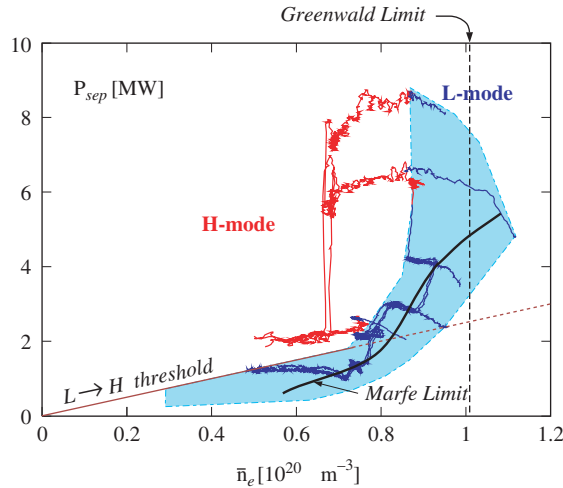


**Figure 4.** The density limit for H-mode operation is associated with and somewhat below the overall disruptive limit. Here, the power threshold for H-mode for the ASDEX Upgrade device, which is plotted against density, can be seen to diverge as the disruptive limit is approached. The solid curves represent trajectories of typical high-density discharges. The L-mode regime is shaded in this figure. ASDEX Upgrade reports a weak power dependence for the L-mode limit [41].

approached, deviating from the linear density scaling usually seen for the power threshold [94, 95]. While some small differences in scaling for the H/L and disruptive limits have been found, it is probably best to think of them as part of the same progression.

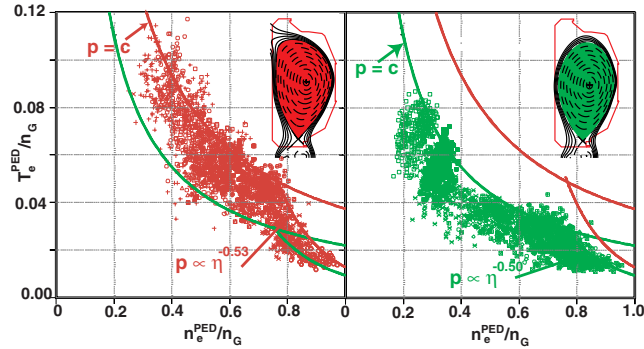


**Figure 5.** Normalized edge temperature is plotted vs normalized density for a sequence of shots from the DIII-D tokamak. The deterioration in H-mode confinement at high density is due to an anomalous drop in temperature below the constant pressure line. Shaping is seen to effect the overall level of the pressure pedestal [102].

The L/H transition and good H-mode confinement are correlated with high edge temperatures [96–100, 91, 101], so it is not surprising that the strong edge cooling associated with the approach to the density limit results in lower confinement and back transitions. Note that this cooling must be stronger than that implied by constant pressure,  $T_{\text{edge}} \sim 1/n_{\text{edge}}$ . With stiff, self-similar temperature profiles ( $\nabla T \propto T$ ), and relatively flat density profiles typical of H-mode, this relation results in total stored energy,  $\int nT dV$ , which is independent of density. Confinement degradation results from situations where the temperature drops faster than  $1/n_{\text{edge}}$  as can be clearly seen in figure 5 from DIII-D [102]. Discharges follow a constant pressure curve until  $n/n_G \sim 0.75$  after which they drop precipitously [102, 50]. No shift to higher densities in the confinement curve is seen as the triangularity is increased; however, the higher triangularity discharges have better confinement and higher pedestals overall. The degradation in H-mode confinement shows considerable variation from experiment to experiment. Plasma shape, particularly triangularity has been found to be an important variable in determining the density at which confinement begins to drop. This is likely connected to the pedestal stability which is predicted to depend on shape. Figure 6 shows data from JT-60U which demonstrates a clear increase in the density at which confinement degradation sets in as the triangularity is raised. (The H factor shown is the ratio of the measured energy confinement time,  $\tau_e$ , to the confinement time predicted by the L-mode scaling law,  $\tau_{\text{ITER89P}}$ .) At low triangularity, the drop can begin as low as  $0.2\text{--}0.4n_G$  with confinement no better than L-mode by  $n/n_G \sim 0.7$  [89]. Confinement degradation was held off to  $n/n_G \sim 0.5$  at higher triangularity ( $\delta > 0.2$ ) [103].

JET has reported a dependence on triangularity with confinement degradation setting in at  $n/n_G \sim 0.5$  for  $\delta = 0.14$  and at  $n/n_G \sim 0.8$  for  $\delta = 0.38$  [90, 32]. The edge temperature was seen to drop, but divertor detachment and MARFE formation did not account for the observed loss of confinement. The drop in edge temperature was correlated with a change in the ELMs which diminished in amplitude and increased in frequency, finally reverting to type III. The effect did not seem to depend on which hydrogen isotope was used (figure 7), input power, divertor geometry or pumping. The drop was correlated with fuelling rate, with the fuelling efficiency reaching zero at the density limit. Radiated power increased but remained below

50% of the input power. The change in confinement has also been correlated to a change in the relative magnitudes of the  $E \times B$  shearing rate and the linear growth rate for ITG modes in the region just inboard of the pedestal [104]. At high densities,  $n/n_G \sim 0.85$ , the balance shifts to the instability growth, implying less stabilization and higher transport. ASDEX Upgrade observed the drop in confinement starting at  $n/n_G \sim 0.4$  at low triangularity ( $\delta \sim 0.2$ ) and at 0.6–0.7 for high triangularity ( $\delta \sim 0.3$ ) [91, 105, 106]. The change in shape also increased the H/L limit by about 20%. Discharges near the density limit had low edge temperatures and could readily be distinguished on an edge operational space diagram from standard H-modes which maintain a constant edge pressure [98]. The pedestal temperature gradient dropped implying a significant increase in  $\chi_{\perp}$ . As the density was raised, the divertor plasma began to detach between ELMs, eventually reverting from type I to type III with confinement

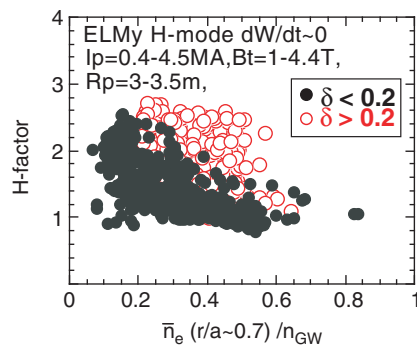


**Figure 6.** H-mode confinement typically degrades at high density. Many devices report an increase in the density at which this degradation sets in for more strongly shaped discharges. Here, confinement data from JT-60U are plotted vs the normalized density [103].

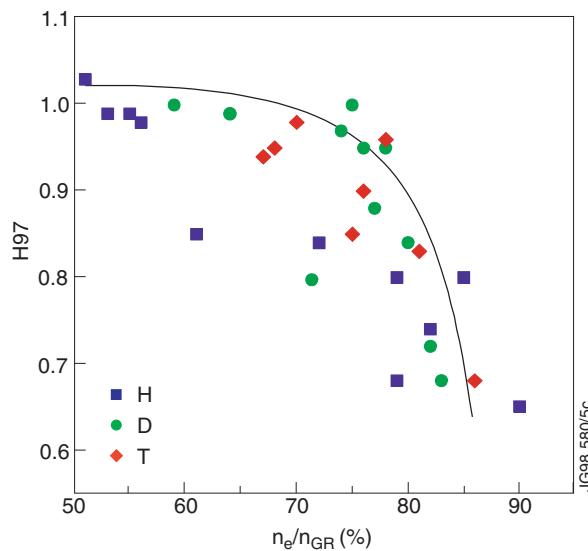


**Figure 7.** H-mode confinement degradation at high densities can be seen in data from JET. These data show that this effect, like the overall density limit, is essentially independent of hydrogen isotope [32].

barely distinguishable from L-mode (though a small pedestal was clearly present). Strong gas puffing increased the density at the separatrix, but the line-averaged density saturated. In C-Mod which ran with  $\delta \sim 0.4$ , degradation began at  $n = 0.65\text{--}0.7n_G$  reaching H89 factors  $\sim 1$  at  $n/n_G \sim 0.85$ , where the back transition to L-mode occurred [107]. Without density profile peaking, DIII-D found that energy confinement began to drop at about  $0.6\text{--}0.7n_G$  [50].

*2.2.1.5. MHD and disruptions.* At the highest densities, the region of cool radiating plasma expands from the separatrix and intrudes into the core plasma. The closed field lines of the core plasma provide a short connecting path resulting in poloidal symmetrization of the radiating layer. In effect, the plasma now rests on a radiating gas mantle rather than on a solid limiter. This process can be stable, resulting in long-lived ‘poloidally detached’ plasmas, but is more often unstable, leading to an uncontrolled contraction of the temperature profile. This has the effect of shrinking the current channel and destroying the MHD stability of the discharge [57, 108]. The growth of MHD fluctuations and the termination of the discharge have been studied numerically [109–115] and experimentally [116, 55, 56, 117–120]. While the details can be complicated, involving nonlinear growth and coupling of numerous MHD modes, the basic process is straightforward. Uncontrolled profile shrinkage leads to unstable current profiles driving resonant modes with large magnetic islands which break up the flux surfaces and connect the plasma directly to the wall. The growth of large islands tends to slow any mode rotation, diminishing the beneficial effects of conductive wall stabilization and accelerating the process [108]. Work from MHD simulations has suggested that skin currents, produced as the current profile shrinks, can drive large internal kink modes [113, 115]. Evidence from tomographic x-ray measurements confirms the intrusion of a ‘cold bubble’ of plasma into the plasma core [117, 121]. The disruption itself proceeds in two steps. In the first step, heat flows along field lines now connected to the wall and quickly cool the plasma in the so-called ‘thermal quench’. The thermal plasma can now no longer support the plasma current which is transferred inductively to the vacuum vessel and support structure or to runaway electrons in the ‘current quench phase’ [57]. The combined effects of heat from the thermal quench or deposition of runaway electrons and mechanical forces arising from induced currents and the toroidal field can damage large devices and are a critical design concern for future reactors [122]. Attempts to influence the evolution with localized heating [119] or ergodic divertors [123] have had only limited success and have not led to higher density limits. Radical changes in wall materials have led to density limiting behaviour without disruptions [37]. In this case, a strong relaxation oscillation sets in at high density involving fuelling, particle balance and radiation.

### *2.2.2. Global scaling*

Introduced in section 1, the first attempts to achieve a predictive capability for the density limit were based on empirical scaling of global parameters. While generally successful, one must keep in mind that this approach misses any local or profile dependences and produces results without a clear connection to the underlying physics. The density profile, unlike the temperature profile, shows no tendency for stiffness or self-similarity and thus may vary considerably. Discharges with significant density peaking are able to reach higher average densities than those with flat profiles. This effect constitutes an important ‘hidden variable’ for global scaling which may attribute its effect to parameters which are correlated with the degree of profile peakedness. It is widely recognized that there are several density limiting mechanisms. For example, plasmas contaminated with large quantities of high  $Z$  impurities have fairly low-density limits due to excessive core radiation. It is desirable to eliminate such

'special cases' from consideration. The underlying assumption (which looks reasonable but which has not been proven) is that there is a common, well characterized limit that can be achieved when all parasitic effects are eliminated by wall conditioning or other optimizations. Under some circumstances, the thermal contraction which precedes the disruptive limit can be stable leading to a poloidally detached state [124, 125]. This usually occurs at densities well below the limit in cases where the plasma contains a large quantity of low  $Z$  impurities. The detached zone can be quite large, e.g. 5 cm out of a minor radius of 26 cm on DITE [67]. Care must be taken when comparing such discharges to empirical expressions as their effective minor radius is smaller than those attached to the wall. In these cases, the plasma is effectively limited by a cool gas mantle rather than a material wall and values for the plasma radius would have to be adjusted accordingly.

Additional difficulties attend the calculation of global scaling laws for the density limit. Operational boundaries may be described in terms of global variables like total current or average density or local variables, like the edge temperature and density and their gradients. The latter are presumably the basis for the underlying physics but are more difficult to measure and not uniformly available from device to device. Moreover, designers of future machines cannot yet predict local parameters from first principles and thus cannot make use of an operational boundary described in terms of these variables. Scaling studies typically combine data from standard operation and a relatively few dedicated sets of experiments. Most experimental operation is carried out far from the limit, so *post hoc* mining of existing databases provides only limited data for these studies. In determining the density limit, it is tempting to draw a boundary to enclose all data points. This procedure, however, gives great weight to outliers and can be misleading. The Greenwald limit was derived so that 95% of the data had  $n/n_G < 1$  [3]. Thus by construction, 5% of the data set used in the derivation exceeded the published limit. This figure was essentially an arbitrary one, based on pragmatic grounds; the scaling expression was derived originally to predict the maximum operating density for a proposed ignition experiment with a reasonable margin of error [126]. Significant covariance among the nominally independent variables often exists as well and frustrates statistical analysis. Since the goal is to obtain a quantitative description of the accessible parameter space. The potential for systematic errors in data and definitions suggests that it is wise not to carry out fits with a large number of parameters or to express the coefficient or exponents with many significant digits.

Given these limitations, the derived scaling expressions have been remarkably successful, perhaps fortuitously. The Greenwald limit was derived from a relatively small set of data, but predicted the density limits (at least for discharges with flat profiles) for a wide range of devices that were subsequently commissioned including FTU [127, 39], JET [57, 40], DIII-D [72], TFTR [128], TUMAN-3 [11], TEXTOR [53, 48], C-Mod [54], START [129, 130], JT60-U [38], TCV [12], ASDEX Upgrade [41], NSTX [15], MAST [27]. The last devices, large spherical tokamaks with aspect ratio  $R/a < 1.8$ , may have a density limit 20–40% higher than  $n_G$ , reasonably good agreement given that the scaling law was derived for machines with a narrow range (3–5) of aspect ratios. Figures 8 and 9 show data from machines that were not part of the original scaling studies and give an idea of the agreement which has been observed. On DIII-D, a series of density limit experiments with L-mode and H-mode plasmas were performed over a wide range of plasma current, field, plasma shape and input power [72]. The basic linear scaling with plasma current was found in scans from 0.5 to 1.9 MA at constant toroidal field and plasma shape. Scans of magnetic field from 0.8 to 2.1 T at fixed current and shape and scans of elongation from 1.1 to 1.9 at constant current found no significant dependences on these parameters. Together, these suggest that there is no explicit dependence on the MHD safety factor  $q$ . Scans of minor radius from 0.2 to 0.67 m found a

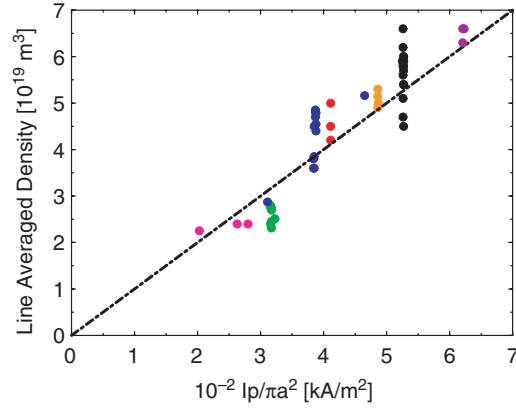


**Figure 8.** Although density limit data from TEXTOR-94 was not part of the set used for the empirical scaling, it is seen to agree well with it. The Greenwald limit is represented by the dashed line [53].

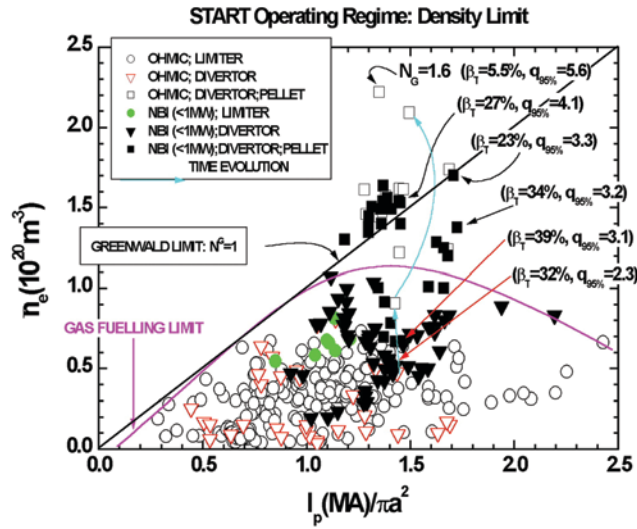


**Figure 9.** Density limit from START also obeys the empirical scaling. With an aspect ratio of only 1.35, this device represents a significant extrapolation from the data set used to derive the empirical scaling. Those data included aspect ratios only in the range 3–5.

slightly stronger dependence than the empirical relation,  $1/a^{2.4}$  rather than  $1/a^2$ .

It may or may not be significant that the commonly used global scaling laws for the density limit are not quite ‘dimensionally correct’. That is, they cannot be constructed from the dimensionless variables believed to be important for plasma physics, namely the normalized pressure, gyro-radius and collisionality,  $\beta = nT/B^2$ ,  $\rho^* = \rho/a$ ,  $v^* = vV_T/a$ . When expressed in this form, the Hugill and Greenwald scalings have a residual  $R^{1/4}$ , for example,

$$\frac{na^2}{I_p} \propto \frac{\beta^{3/4} v^{1/4} R^{1/4}}{\rho^{*1/2}} \quad (2.1)$$

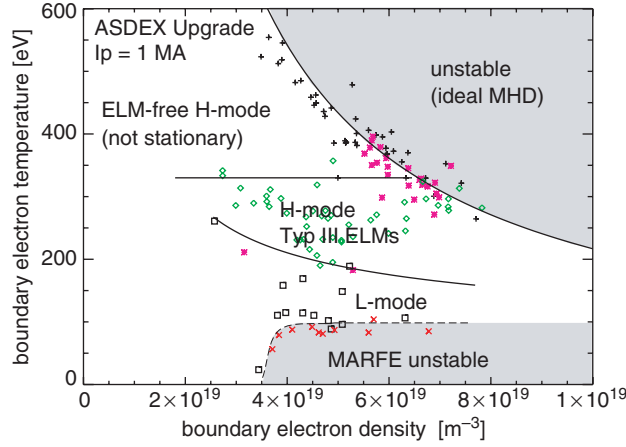


**Figure 10.** The density limit (and other regimes) are classified here in a plot showing edge temperature vs edge density from ASDEX Upgrade. Here the density limit is seen to occur when the edge temperature falls below a threshold [98].

Simple modifications of the expression for  $n_G$  could make it dimensionally correct, for example,

$$n \propto \left( \frac{I_P}{a^2} \right)^{8/9} \quad \text{or} \quad n \propto \frac{I_P}{a^{7/4}} \quad (2.2)$$

However, both differ from the original form by a factor of about 1.5 when evaluated across the current tokamak database, and would not be consistent with data and estimated errors. The expression could be made dimensionally correct by inclusion of other dimensioned variables, an exercise which would require compilation of a significant database and great care over data conditioning and covariance. (Note that even with much larger and better conditioned data sets, the unconstrained energy confinement scalings are only slightly more dimensionally correct [4].) Alternately, there may be additional important non-dimensional parameters, e.g. those connected with atomic physics processes.

The empirical law discussed above does not describe the results of all experiments. In particular, it fails badly in those cases where the density profile is peaked. It is not surprising that an expression based on a global quantity like the line-averaged density is unable to capture profile effects. The observation that discharges with peaked density profiles can routinely exceed the empirical limit confirms the hypothesis that the physics underlying the density limit is to be found in the edge plasma. A more complete discussion of profile effects on the density limit can be found in section 2.2.3 below. Recent experiments from low aspect ratio tokamaks indicate that there may be higher order effects due to extreme shaping [15, 27]. New data, particularly from machines like MAST, NSTX, and TCV, will help clarify these issues. Caution must also be taken when extrapolating an empirical law far from the parameter ranges of the data from which it was constructed. The empirical law also fails to capture the weak power dependence which has been observed in some experiments (see section 2.2.4). Since these results are in machines heated by neutral beams, some care must be taken to separate the effects of heating and fuelling—noting that a future reactor would not have a strong central fuelling source.

### 2.2.3. Effects of density profile on the limit

While the empirical law for the line-averaged density,  $n_G$ , described above, has been

successful for a wide range of experiments and configurations, the density limit can be extended by operating in regimes where central fuelling, edge pumping, or modification of particle transport lead to peaked density profiles. Peaked density profiles have long been associated with the suppression of anomalous transport [131–137] resulting in self-sustained regimes with improved confinement and very high central densities. Studies of pellet fuelled discharges yielded densities 1.5–2 times the limit compared to those fuelled at the edge by gas [43, 44, 46, 47]. Cryopumping [47], impurity puffing [45, 48] or spontaneous transitions [49, 50] can also lead to peaked density profiles and higher density limits. A systematic investigation on ASDEX included discharges where the density was peaked via pellet injection, NBI and transport modification [138]. In these experiments, the edge density stayed below the empirical density limits, the increase in line average coming from particles in the plasma core. This was consistent with models which attribute the density limit to physics in the plasma edge. Further experiments on ASDEX showed a critical edge temperature for density limit disruption [9]. Figure 10 shows data from ASDEX Upgrade, supporting the idea that the operating regimes can be defined in terms of edge temperature and density. Particles added to the central plasma apparently don't induce density limiting phenomena.

If the central fuelling is increased by very strong NBI and the edge source reduced through wall pumping, peaked density profiles can be produced. Early NBI work on DITE with gettered walls showed highly peaked profiles with peak to average values up to three [22, 6, 23, 24]. Essentially, all the fuelling in this case could be attributed to the beams. TFTR was able to reach  $1.2n_G$  in L-modes with strong neutral beam heating [128], while in ASDEX Upgrade experiments with NBI, the disruptive density limit was raised to  $1.4n_G$ . DIII-D has carried out a series of studies aimed at exploring regimes with good H-mode confinement above the empirical limit [47]. By a combination of cryopumping in the divertor and beam fuelling, densities up to  $1.4n_G$  were obtained. Peak to average densities in this case were around 1.3. Good confinement ( $H_{89} \sim 1.9$ ) was maintained despite a sharp decrease in edge pressure [50]. This deterioration was attributed to the loss of second stability brought about by a drop in bootstrap current at higher collisionality. Average confinement was maintained by an improvement in the core, likely the result of the peaked density profile. Achieving these conditions was difficult for several reasons: low edge confinement produced MARFES increasing the fuelling demand; the increased fuelling rate led to divertor collapse; raising the magnetic field increased the L/H threshold, limiting the available operating space. The density peaking and good confinement were not sustained at high power, limiting the regime to a narrow operating window [49].

Density peaking can be accomplished most directly by deep pellet fuelling [133] and can easily lead, at least transiently, to line-averaged densities in excess of  $n_G$  [139, 3, 140, 38]. By repetitive injection of small pellets, ASDEX was able to reach  $1.5n_G$  in a quasi-steady state [43, 9]. The edge densities measured on that device remained well below the limit [9]. TFTR obtained a similar result, reaching  $2n_G$  by injection of six large deuterium pellets [128]. ASDEX Upgrade has reached equal levels of performance with low-field launch [141] and high-field launch [142, 60], the latter showing much higher fuelling efficiency even with lower velocity pellets. High-field launch also enabled operation in H-mode with good confinement at densities up to 1.5 times the limit [68]. Figure 11 shows time traces of the normalized confinement time and normalized density from experiments on DIII-D [143, 144]. A divertor cryopump was used to reduce the neutral density, keeping the edge temperature from falling, thus avoiding divertor detachment (X-point MARFES). The good confinement could not be maintained with NBI power above 3 MW. It is possible that the additional heating power increased the core particle transport and destroyed the peaked profiles. Figure 12 shows the multi-variate dependence of density, density profile and triangularity on H-mode confinement [102].

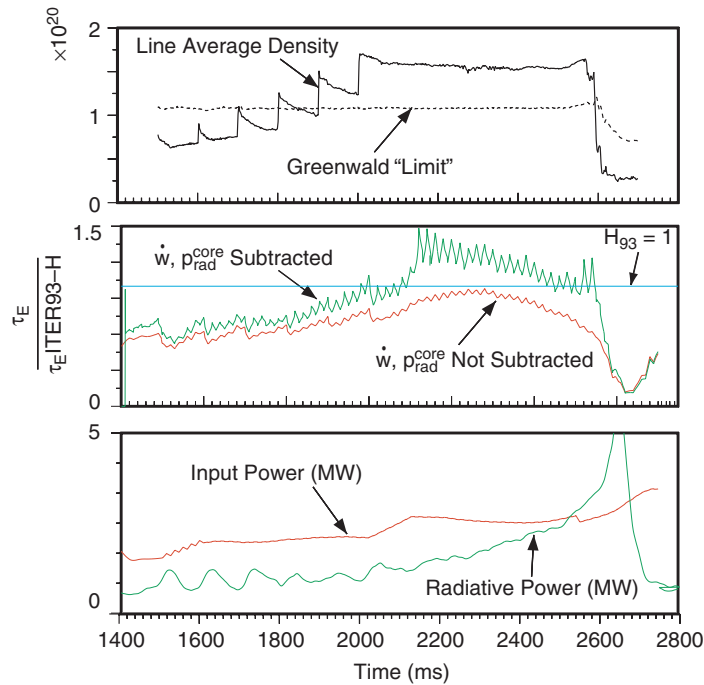


**Figure 11.** Discharges with good confinement are achieved at densities above the empirical limit by pellet fuelling in DIII-D. Because the density limit is due to edge physics, plasmas with peaked density profiles can reach higher average densities than those with flat profiles. In these discharges, confinement is enhanced over L-mode in part due to the improved core confinement associated with peaked profiles. The concomitant accumulation of impurities leads to a strong increase in radiation and discharge termination [143].

It is also possible to obtain peaked density profiles by modifying particle transport. While this is usually accomplished in discharges with some central particle source from neutral beams, it has also been demonstrated in Ohmic and RF-heated plasmas with no core fuelling whatsoever [145, 146, 39, 147]. The physics which initiates this transport modification is not well understood, but is generally thought to be due to a drop in ITG growth rate via modification of the ion density profile [148, 147]. The peaked pressure profiles that result can be sustained via suppression of turbulence via sheared plasma flows [149]. Another possibility is that off-axis heating in the context of marginally stable turbulence can lead to low diffusivity on-axis. In the presence of even a small particle pinch, peaked profiles could result. The radiation enhanced mode (RI-mode) provides the most abundant examples of high-averaged densities achieved in steady state discharges with peaked profiles [74, 45, 150–152, 48, 14, 153, 154]. Both particle and energy confinement were improved allowing achievement of H-mode like confinement at densities up to  $1.5n_G$  [155]. (The comparison with H-mode is for illustration only; these discharges have improved confinement via an internal rather than edge transport barrier.) The RI-mode does not seem to be degraded by input power and the achieved densities are often the highest at high power. A similar regime has been observed in ASDEX Upgrade but includes an H-mode edge barrier [88]. Dubbed CDH for CDH, this regime is produced by neon puffing which creates a mantle of cold radiating plasma. It combines good confinement, high density, somewhat peaked profiles and a drop in power loading on the divertor plates [156, 98].

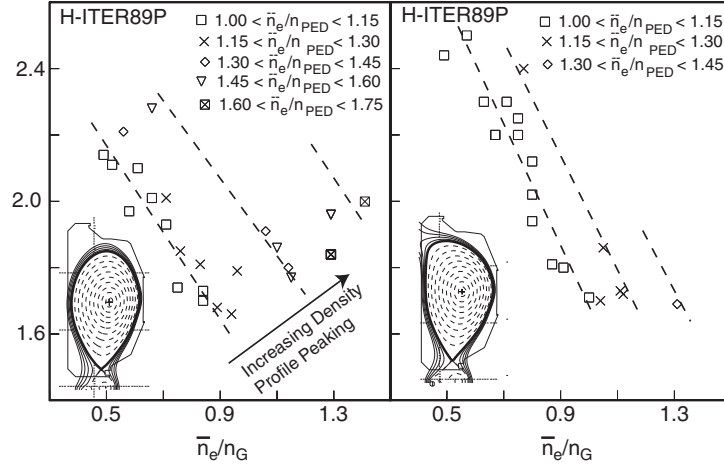


**Figure 12.** Energy confinement normalized to the ITER89 scaling law is plotted against normalized density for discharges with different degrees of density peakedness from a set of discharges in DIII-D. The improvement in overall confinement for plasmas with peaked density profiles is particularly marked at high densities. The deterioration in confinement at high densities can also be seen and is found to be mitigated by stronger shaping [102].

Operation with peaked density profiles does not eliminate the edge limit, it simply allows operation at higher averaged or peak density. This points out the care that must be taken when using global parameters like  $\bar{n}_e$  and  $\tau_e$  to characterize what is essentially local physics. Extrapolation of these results to reactor regimes is attractive but uncertain. In principle, operation with peaked profiles can allow almost arbitrarily high central densities, limited only by MHD stability constraints on the pressure profile. On the other hand, they are based either on fuelling approaches which may not scale to very large devices or on transport control techniques with incompletely understood physics. Core transport tends to degrade with additional heating power, limiting these regimes mostly to low power so far. In experiments with NBI, heating and fuelling are progressively farther off-axis as the density is raised. With alpha heating, the power will be centrally peaked and provide no fuelling. There are indications from current experiments that this could lead to flat profiles [157]. Shear-flow stabilization would seem to be more problematic as  $\rho^*$  drops to the values characteristic of a reactor.

#### 2.2.4. Power dependence

The empirical limit,  $n_G$ , does not include any dependence on input power or plasma purity. Early work on NBI heating found that while higher densities were reached with auxiliary power, the ratio of  $n/I_p$  was constant [24]. Studies that led to the Greenwald empirical density limit had found no significant dependence on power in a database from the Alcator-C, Doublet III, ISX, PBX, and PDX. Experiments on DIII-D (figure 13) confirmed this observation over a range in input powers up to 8 MW [72], though more recent work on DIII-D found a dependence of  $P^{0.1}$  [46]. On ASDEX, power scans at  $q = 2.9$  found a significant dependence with  $n_{\text{limit}} \sim P^{0.25}$  [7, 9]. The power dependence was stronger at  $q = 2$ , though these discharges are near the current limit as well and could not attain densities as high as plasmas with larger  $q$ . ASDEX Upgrade investigated the H/L density limit, deriving a scaling with field, power and  $q$ ,  $n_{H/L} = 5.0 P_{\text{sep}}^{0.15} B^{0.61} / (qR)^{0.95}$ , where  $P_{\text{sep}} = P_{\text{in}} - P_{\text{rad}}$  [92, 105]. A somewhat larger power dependence,  $P^{0.3}$ , was seen on the L-mode disruptive limit resulting in a greater

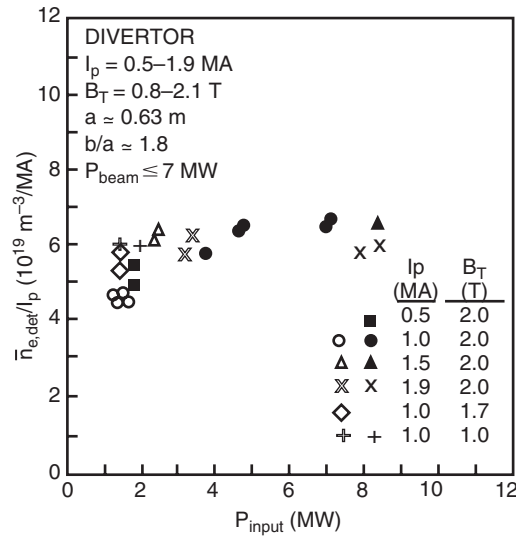


**Figure 13.** The normalized density at which divertor detachment occurs is plotted vs input power over a very wide range. These data, taken from DIII-D, are very close to the disruptive density limit. Essentially no power dependence is seen [72].

separation between the two limits at high power [68, 41]. Overall, it must be concluded that compared to the expectations from arguments based on power balance, the density limit is not found to increase strongly with input power. This result has significance for the extrapolation into the reactor regime. Since, like radiated power, fusion power scales with  $n^2$ , mechanisms based entirely on impurity radiation imply no real density limit for ignited plasmas [16].

Most studies of the power scaling of the density limit have been in experiments with neutral beam heating. For these cases, the role of core fuelling by the beams must be considered. The ionization source from the beams is always much smaller than that from gas impinging on the plasma edge. However, it would not be correct to conclude from this that the beams are not important in the particle balance. Low-energy neutrals from molecular dissociation of hydrogen gas do not penetrate deeply, often ionizing on open field lines in the SOL. As a result, the efficiency of gas fuelling is typically 10–30 times lower than beam fuelling [38]. This difference may become greater as the density limit is approached. Particle transport experiments in JET have compared NBI and ICRF heated plasmas [158] finding that beam heated discharges had somewhat higher average densities and mildly peaked profiles when compared to those heated by RF. The difference was attributed to a change in particle source rather than any change in transport. Alcator C-Mod, which uses ICRF as its only auxiliary heating scheme, sees no dependence of the density limit on input power.

### 2.2.5. Impurities, isotope dependence, and wall conditioning

The achievable density in a tokamak is clearly reduced when the plasmas are heavily contaminated by impurities. Wall conditioning has become a standard technique for increasing the accessible range of densities. Analysis of an early multi-machine database found that the operational space contracted as  $Z_{\text{eff}}$  was increased from 1 to 8.5 [159]. Achievable densities for the dirtiest plasmas were less than half of those which could be obtained at  $Z_{\text{eff}} \sim 1$ . Studies on Alcator-C found that the density limit was reduced only for  $Z_{\text{eff}} > 2.5$  [3]. In ASDEX, the greatest effects of wall conditioning were seen for  $Z_{\text{eff}} > 2.5$ . The increase in

achievable density when  $Z_{\text{eff}}$  was lowered from 2.5 down to 1 was 15% at most [9]. FTU was able to reach the empirical limit after a program of baking and discharge conditioning cleaned the metallic walls of that device [127]. On TEXTOR, studies with auxiliary heating found that poloidal detachment followed by major disruptions occurred at  $n/n_G \sim 0.75$  for  $Z_{\text{eff}} \sim 5$  and dropping to  $n/n_G \sim 0.3$  at  $Z_{\text{eff}} \sim 10$ , consistent with a model for radiative/thermal collapse. However, for  $Z_{\text{eff}} < 2.5$ , densities up to the empirical limit could be achieved (figure 14) with no dependence on  $Z_{\text{eff}}$  below this value. Experiments with auxiliary heating are crucial for these studies, since the increase in  $Z_{\text{eff}}$  is accompanied by an increase in Ohmic heating power, entangling the effects of these two parameters. Lowering the atomic number of the impurities is a clear advantage, since this typically results in less power lost through radiation. Covering the walls with a layer of boron enabled operation of clean plasmas even at high input power. With uncovered metallic walls the achievable density can be much lower [10]. TCV has also shown a clear increase in the accessible density following boronization [160]. In JET, when graphite first wall components were replaced by beryllium, there was no plasma contraction and no disruption, though the density limit remained roughly the same. Instead, a relaxation oscillation set in, involving radiation, fuelling rates and MARFE formation [37].

For some circumstances, introduction of impurities may have a beneficial effect on the plasma, allowing good energy confinement at densities at or somewhat above the empirical density limit [152]. This phenomenon was first reported by the ISX-B group as ‘Z-mode’ [161, 162]. In these experiments, a small amount of neon was puffed in neutral beam heated discharges resulting in peaked density profiles and somewhat improved energy confinement. These early results have been extended and explored extensively on many devices, particularly by the TEXTOR group [163, 132, 45, 150] which has referred to the regime as RI-mode, for radiative improved confinement mode. In addition to impurity puffing, RI-mode requires operation at high densities with low recycling walls. Plasmas obtained by this recipe have energy confinement which increases roughly linearly with density and have moderately peaked density profiles. The result is reminiscent of the improved confinement regime obtained by pellet injection [164, 131] and has been attributed to a similar mechanism, namely the

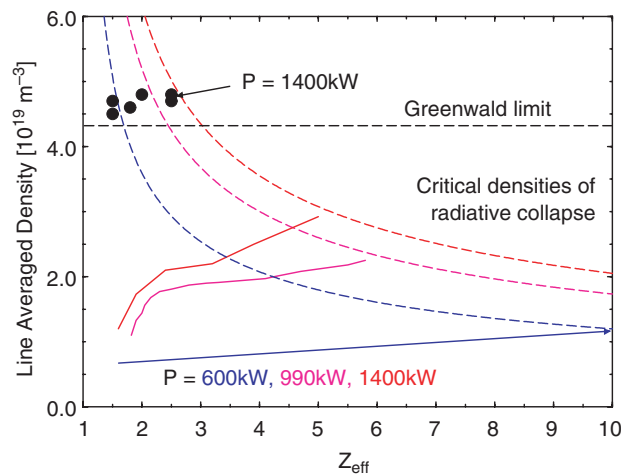


**Figure 14.** The solid curves show time histories of density vs  $Z_{\text{eff}}$  for a series of TEXTOR discharges taken at different levels of input power. For the higher values of  $Z_{\text{eff}}$ , the shots terminate on curves (---) calculated for a radiative collapse. Below  $Z_{\text{eff}} \sim 2.5$ , an impurity independent limit is found which coincides with the empirical scaling [53].

suppression of ITG modes [165].

The hydrogen ion isotope is not found to be particularly important for the density limit. TEXTOR reported slightly higher limits in deuterium and slightly more peaked density profiles as compared to hydrogen [166], while JET found no significant difference as the tritium content was raised [167]. ASDEX has reported significantly higher density limits for helium discharges compared to deuterium, particularly at low current where the helium discharges had very peaked density profiles [9]. NSTX has recently reported higher density limits with helium as well [15].

### 2.2.6. Fuelling effects

Though many studies have focussed on power balance, it is important not to overlook the role of particle balance in the density limit. Gas fuelling becomes less and less efficient and the neutral pressure surrounding the plasma grows exponentially as the density is raised [168, 169]. Studies of high-density operation in ASDEX Upgrade found that the central density didn't respond at all to increases in gas puffing, while the separatrix density increased only weakly and the SOL density increased strongly [41]. This general behaviour is due at least in part to the decline in neutral penetration that occurs at high density. Above about 10 eV, the ionization and charge-exchange processes that limit neutral transport are not strong functions of temperature, yielding a mean free path (and thus the plasma source rate) for neutral penetration which is proportional to  $1/n_e$ . The plasma 'self-shields', causing ionization to occur further out in the plasma edge and lowering fuelling efficiency. (Note that this is not particularly an issue of machine size, but may depend more strongly on the magnetic field. If the figure of merit for neutral fuelling is the neutral mean free path,  $\lambda_{no}$ , divided by the minor radius,  $a$ , then at the empirical density limit  $\lambda_{no}/a \sim 1/B_p$ ). A drop in fuelling efficiency nearly to zero as the limit was approached has been reported in FTU [39] and JET [32]. A drop in the observed density limit for the MIIa divertor in JET was blamed on the lower fuelling efficiency achieved with a closed divertor. While it is clear that the efficiency of fuelling is higher for more deeply deposited particles [38], fuelling dynamics also depends critically on particle transport which is only poorly understood. It is not clear at this point whether the drop in neutral penetration or changes in particle transport is more important in reducing fuelling efficiency at high density.

There are practical limits to machine operations at very high neutral densities. As the fuelling efficiency drops, each ion which ends up in the plasma requires more interactions at the plasma edge. Since each ionization and charge-exchange event causes energy loss, the process may ultimately be unsustainable. JET reported a drop in H-mode confinement which was correlated with the lower fuelling efficiency of their Mark IIa divertor configuration [40, 170]. Machine geometry, the choice of wall materials and vessel conditioning can all play an important role in the neutral dynamics of experiments. Materials with a strong affinity for hydrogen can lower the density through strong wall pumping. Note that in future long pulse or steady state experiments, the walls will saturate and should cease to be a variable in the fuelling processes.

Overall however, observations suggest that the density limit as embodied by  $n_G$  is not due to a drop in neutral fuelling by itself. For example, in cases where the neutral density is held down by strong wall pumping, the standard limit can be recovered by alternate fuelling techniques [171, 172, 37]. Beam and pellet fuelling alter the particle balance by moving the source into regions of lower transport. The core particle confinement time is typically measured to be the same order of magnitude as the global energy confinement time, much higher than the global particle confinement time which is dominated by edge recycling. The limitations of gas fuelling relative to that of high-energy neutral beams may account for the lower density limits reported at high current in DITE [6] or during early operation of JET [173], where significant power scaling was seen as well, but only with NBI. ICRF heated discharges had density limits

similar to those seen with Ohmic heating alone. Beams or pellet fuelling can also lead to more peaked density profiles which may allow operation at central densities higher than the empirical limit. Studies in JET showed much flatter profiles for ICRH,  $n(0)/n_{\text{edge}} \sim 1$  than for NBI which had  $n(0)/n_{\text{edge}} \sim 1.2\text{--}1.3$  [158]. This difference was most apparent at high densities, as would be expected.

### 2.3. Reversed field pinch

As in a tokamak, the RFP has a poloidal field produced by toroidal current flowing in the plasma and a toroidal field produced by external coils. The two fields are of roughly equal strength in an RFP, resulting in bad local and average curvature. To provide stability, the toroidal field is reversed near the plasma edge creating very strong magnetic shear. Consequently, the MHD and transport properties can be rather different from those in a tokamak. In modern RFPs the field reversal is maintained through a turbulent dynamo effect permitting relatively long discharge times. In general, the density limit in RFPs is characterized by an increase in fluctuation levels and a slow decay of the plasma current [174, 175]. In RFX, fast termination has also been observed for  $I_p > 0.9$  MA [13]. The fast termination begins with a thermal quench, loss of field reversal and finally to the loss of plasma current. At lower plasma currents, only the slow termination is observed. While there have been only a few dedicated studies of the density limit in the RFP configuration, sufficient data exist for quantitative comparisons between RFPs and tokamaks. Note that plasma heating in most RFP experiments is through Ohmic dissipation alone so it is not possible to separate, with certainty, effects due to power balance from those linked to the magnetic field strength.

In the RFP literature, the operating range has been parameterized by the ratio  $I/N$ , where  $I$  was the toroidal plasma current and  $N$  was the density of particles per unit toroidal length [176]. Simple algebra shows that for a circular, high aspect ratio device, this parameter is equivalent to  $\pi a^2 I_p / \bar{n}$  which is proportional to  $n_G/n$ , the inverse of the normalized density using definitions from section 1.1. An ‘optimum range’ for RFP operation was reported on ETA-BETA II with  $I/N \sim (1\text{--}1.5) \times 10^{-14} \text{ A m}^{-1}$  [176] corresponding to  $n \sim 0.6\text{--}1n_G$ . Extensive heating and confinement studies were carried out in this device with  $n \sim n_G$ . The quantitative similarity in the density limits between the two devices was noted in papers which suggested that a similar mechanism might be at work for both [26, 25, 177]. Other RFPs have reported operation in the same density range, e.g. HBTX1A operated at  $0.2\text{--}1.0n_G$  [178], OHTE, which incorporated helical windings into the RFP configuration, reached  $\sim 1.0n_G$  [179]; ZT-40M  $\sim 0.6n_G$  [180]; MST  $\sim 0.5n_G$  [181]. It is an interesting historical note that the earliest reports of ‘quiescent’ behaviour in the Zeta device described operation at  $0.8n_G$  [182].

Linear scaling of plasma density with current was found in TPE-1R(M), but at values of  $I/N$  that were about 10 times higher than that reported in other devices [183]. ETA-BETA II reported linear scaling of the limit at  $n \sim n_G$  over a range in plasma current from 0.1 to 0.22 MA [184]. Perhaps the most comprehensive work on density limit scaling in the RFP has been carried out recently by the RFX group (figure 15 [13]). In these experiments, the limit matched the Greenwald scaling within about 15% over a wide range in plasma current for both ‘soft’ and ‘hard’ terminations, similar to tokamak disruptions. The ‘hard’ limit was seen only for current densities higher than  $1.2 \text{ MA m}^{-2}$ , while the ‘soft’ limits occurred at all densities. Pellet fuelling in RFX allowed the limit to be overcome, but only transiently. The  $I/N$  ratio has proved to be a good scaling quantity for other phenomena in the RFP, including the plasma  $\beta$ ,  $Z_{\text{eff}}$ , energy confinement [185, 36] and the low-density limit [174, 175]. Poor performance at low density (high  $I/N$ ) has been attributed to instabilities driven by large values of the streaming parameter  $V_{\text{drift}}/V_{\text{thermal}}$  [174].

Radiation is seen to increase sharply with density in RFX, but rarely goes beyond 20–30% of the input power (figure 16 [186]). Analysis of the local power balance showed that radiation played only a minor role everywhere in the plasma. Coating the walls with a thin film

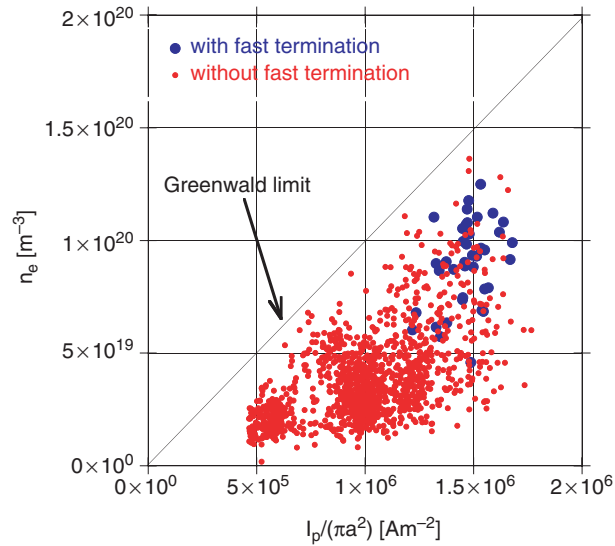


**Figure 15.** An operating space diagram for the RFX RFP. The density limit in this configuration is apparently identical in scaling and magnitude to that of the tokamak. At higher values of current density, fast terminations, which are similar in some ways to tokamak disruptions, are observed [13].

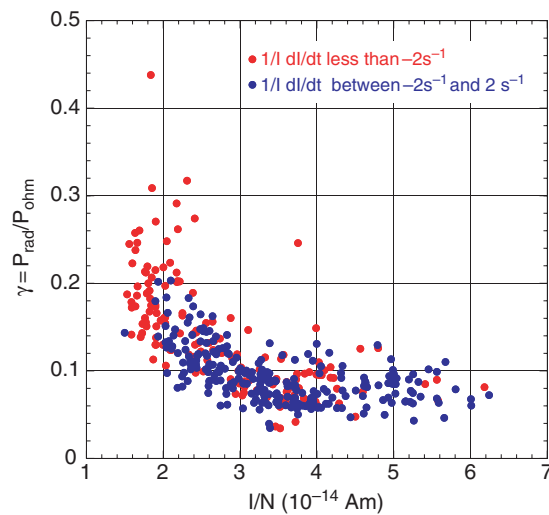


**Figure 16.** The ratio  $P_{\text{rad}}/P_{\text{in}}$  is plotted vs  $I/N = n_G/n$ . While the radiated fraction increases at high densities, it always remains well below 1 [186].

of boron reduced radiated power still farther and allowed slightly higher densities to be reached. Discharges with neon impurities deliberately added have higher levels of radiation, but essentially the same density limit [187]. These discharges are apparently not subject to fast

termination even at high current. Earlier researchers on ETA-BETA II had reported somewhat contradictory data, first suggesting that radiation is always low—of the order of 20% of the input power—though rising with density [176], then later concluding that operation at high density was associated with excessive radiation losses from low  $Z$  impurities, principally oxygen [26]. The lack of a clear result on this point may have been the result of the rudimentary diagnostics and short discharge times that prevailed at this time. In the same time frame, radiation was found not to be a major component of power losses carrying out only about 10% of the input power in HBTX1A [178] and accounting for only about 50% of the input power in OHTE [179]. The low fraction of radiated power suggested that this mechanism is not responsible for the density limit in RFPs, however the precipitous increase as the limit was approached leaves the question unresolved.

#### 2.4. Stellarators

Unlike the tokamak or RFP, which are toroidally symmetric, stellarator equilibria are fully three dimensional. The rotational transform, which is necessary for toroidal confinement, is produced by external coils resulting in greater flexibility in design though with perhaps less flexibility for an operating experiment. Despite the obvious differences between the configurations, stellarators and tokamaks show many similarities in their physics and operating regimes [188] and in their edge turbulence [189].

##### 2.4.1. Behaviour at limit

With no plasma current, the feedback between the temperature profile and MHD stability is not strong in stellarators, thus the density limit is not accompanied by a disruption as in tokamaks. Instead, a ‘soft’ limit or quench is encountered with the plasma temperature decaying away on a confinement timescale [190, 8]. Typical thermal quench behaviour can be seen in traces from the Wendelstein 7-AS (W7-AS) device in figure 17. If gas puffing is reduced, it is possible for a stellarator to recover from the quench [8, 191]. The density limit in an early stellarator, CLEO, was found to be associated with energy losses from radiation by low  $Z$  impurities [192], though the densities obtained in this experiment, of the order  $0.6 \times 10^{20}$ , were well below those achieved in modern machines. Densities approaching  $3 \times 10^{20}$  were achieved in the W7-AS device following boronization [188] and extended to  $3.5 \times 10^{20}$  with the installation of an island divertor [193]. In these experiments, thermal collapse could be triggered by strong gas puffing or by lowered heating power in an established high-density discharge. During the collapse, a large increase in radiation from partially ionized low  $Z$  impurities was observed similar to MARFE or poloidal detachment phenomena. While these observations suggested an important role for radiation in the limit, total plasma radiation was found to be significantly less than the input power [8]. The inference was that local rather than global power balance was the determining factor. By contrast, values of  $P_{\text{rad}}/P_{\text{in}} \sim 1$  were reported in Heliotron E [194]. Pellet fuelling in this device allowed attainment of high-density quasi-steady discharges; however, these were still subject to the collapse phenomena which led to rapid loss of both energy and particles. More recent data from W7-AS also show the collapse occurring when total radiation and input power are balanced [191]. In these cases, the plasma density and radiation profiles were peaked, with core radiation from higher  $Z$  elements predominating. In H-mode, ELMs were capable of reducing impurity content by lowering particle confinement.

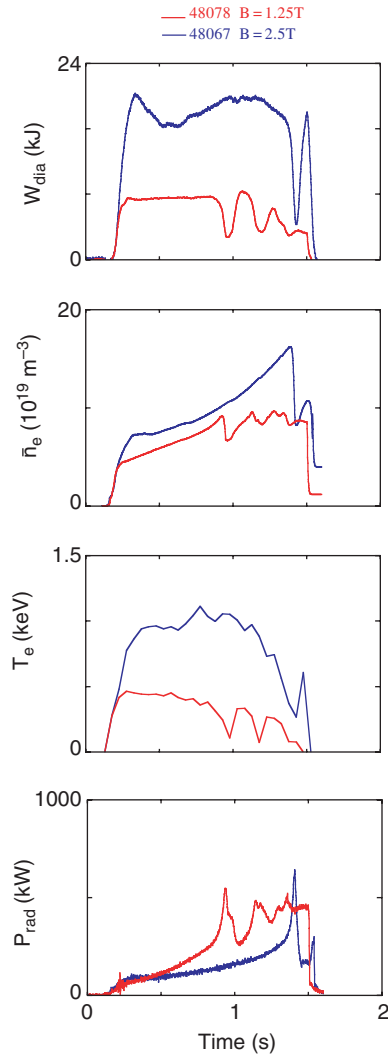


**Figure 17.** A series of traces from studies of the density limit in the W7-AS stellarator. The limit is manifested as a relatively slow thermal collapse, which is clearly visible in the electron temperature and stored energy. At higher magnetic fields, the collapse sets in at higher densities [191].

While ELM-free H-modes proceeded to a radiative collapse, ELMy H-modes could reach a quasi-steady state equilibrium.

#### 2.4.2. Empirical scaling

Since the density limit in stellarators is not associated with disruptions, the maximum density used for scaling studies is typically the value at maximum stored energy—i.e. before the density limit quench sets in. Early attempts to find an empirical law for the density limit in stellarators were based mostly on data from Heliotron E [194, 190]. The result was

$$n_{\text{lim}} = 0.25 \left( \frac{P_{\text{in}} B_T}{a^2 R} \right)^{0.5} \quad (2.3)$$

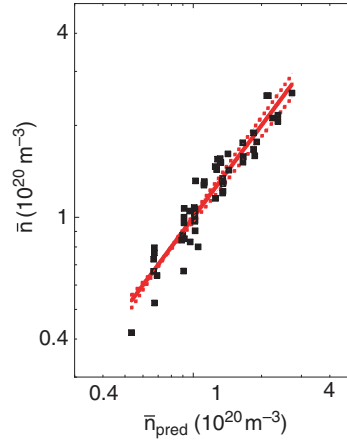


**Figure 18.** A power law fit for the density limit in W7-AS. The scaling relation is  $n_c = 1.46(P/V_p)^{0.48} B^{0.54}$  [191].

consistent with the general observation of strong power and field scaling in stellarators. This fit was compared to data from the L2 and W7-AS stellarators and very rough agreement was obtained. A slightly better fit was obtained with an alternate formulation used for plasmas at low density or with low power:

$$n = \min \left\{ 0.25 \left( \frac{PB}{a^2 R} \right)^{0.5} \text{ and } \frac{0.35 PB^{0.5}}{aR} \right\}$$

Data from ATF were later found to be consistent parametrically with the first scaling but with a coefficient roughly 50% higher [195]. Data from experiments with ECH had a lower density limit, suggesting an effect of beam fuelling or profile shape (these discharges had hollow density profiles). The W7-AS also found higher densities than that given by [190], and produced a number of scaling relations which evolved over the years as more data were collected,  $n \propto P^{0.5}$  [8],  $n \propto B/R^0$  [188] and  $n \propto P^{0.4} B$ ,  $n = 1.46 P^{0.48} B^{0.54} / (a^2 R)^{0.5}$  [191]. An example of scaling results can be seen in figure 18. In [188], data from W7-AS and CHS were compared to obtain the null size scaling. Discharges from W7-AS with values of the rotational transform  $t = 1/q$  ranging from 0.33 to 0.53 were also compared and no significant trend was found (figure 19). Recent data taken with gas fuelling on the large helical device (LHD) were generally consistent with equation (2.3) [196]. With pellet fuelling, densities roughly twice as high were achieved. Taking all studies into account, the exponents for a power law fit range from  $P^{0.5 \rightarrow 1.0} B^{0.5 \rightarrow 1.0} / R^{0 \rightarrow 1.5}$  with the bulk of the data favouring  $(PB/V)^{0.5}$ . The data sets which were used for all of these studies were small and covariance between variables used for fitting or profile effects may be responsible for the different results obtained.

#### 2.4.3. Comparison with tokamaks

Perhaps the most notable result is that power scaling is significantly more important than on tokamaks. Analysis of data from the W7-AS stellarator and the ASDEX tokamak allowed direct comparison between the two configurations [8]. The two machines were similar in size (ASDEX:  $R = 1.65$  m,  $a = 0.4$  m; W7-AS:  $R = 2.0$  m,  $a \sim 0.18$  m) and could be run at the same rotational transform,  $t \sim 0.33$ . Two conclusions can be immediately drawn as seen in figure 20. First, the power scaling for the stellarator was much stronger than for the

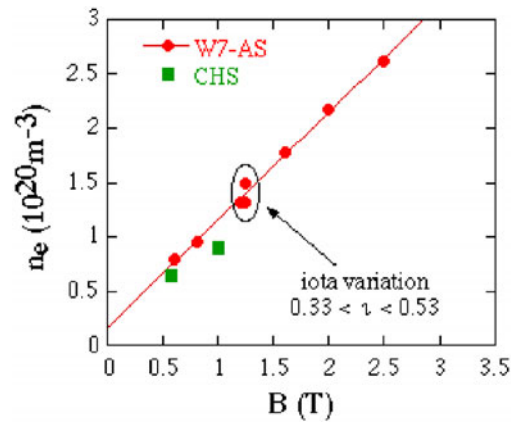


**Figure 19.** The scaling of density limit data from CHS and W7-AS vs magnetic field. Note the lack of size scaling and the absence of dependence on the rotational transform  $\iota$ . These data would lead to a scaling law of the form  $n_c \propto B^1/q^0 R^0$  [188].

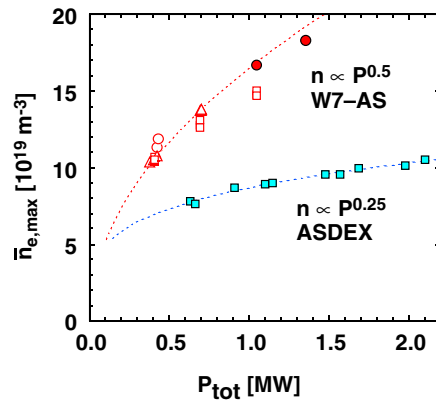


**Figure 20.** A comparison of the density limit scaling in a tokamak (ASDEX,  $B = 2.1$  T,  $1/q = 0.34$ ) and a stellarator (W7-AS,  $B = 1.28$  T,  $\iota = 0.33$ ). The most notable difference is the stronger dependence on input power in W7-AS. Despite the higher field in the tokamak, the stellarator reaches higher density [8].

tokamak (note that ASDEX itself showed stronger power scaling than most other tokamaks.) Secondly, the densities achieved in a stellarator of comparable size and field were significantly higher than those of the tokamak. Some caution should be noted on this point. The use of the rotational transform for comparison is a reasonable and practical method for comparison of the two configurations, however, as seen above, the density limit in tokamaks does not strictly scale with  $1/q$ . The difference (which is the difference between the Hugill and Greenwald scalings) was due to consideration of plasma shaping. The stellarators under consideration all have strong shaping by any measure. Further, note that studies of the density limit in W7-AS found no evidence for strong  $q$  scaling [188]. However, even with these cautions in mind, it seems for at least the current generation of machines, that with devices of a given size and magnetic field and a standard degree of plasma shaping, a stellarator is able to operate at higher densities than a tokamak, perhaps by a factor of order 2. It is not clear if this difference is due

to a fundamentally different mechanism for the limit in the two machines or is a reflection of their different response to the same mechanism.

### 2.5. Spheromaks and field-reversed configurations

Spheromaks and field-reversed configurations (FRCs) are compact toroidal devices in which the plasmas do not link external coils as they do in tokamaks, stellarators, and RFPs. In addition to the engineering advantages that this configuration might bring, both have the potential to run at high beta. In the spheromak, toroidal, and poloidal plasma currents flow mainly along the field lines in a force-free configuration. The FRC is formed by reconnection from a linear theta pinch with a reversed bias field. The FRC is usually highly elongated axially and has only poloidal fields. Both configurations have been produced in short pulsed experiments that have emphasized creation and verification of the basic equilibrium. Discharges in spheromaks typically last for only a few ms and those in the FRC, not much more than 1 ms. Heating in both configurations is through Ohmic dissipation of the confining fields. With pulse lengths short compared to transit times for room temperature molecules, the densities achieved in these devices correspond to the static fill pressure multiplied by magnetic compression effects. Because of the lack of dedicated density limit experiments and the transient nature of the discharges, it is far from clear how to interpret these results within the framework introduced for tokamaks, stellarators and RFPs. Certainly the data available do not represent density limits but rather an optimized operating point. Typically the fill pressure is varied until a range of reasonable performance is achieved. However, as shall be seen, these operating densities are reasonably well predicted by the scaling laws previously discussed.

Data taken from the spheromak CTX is shown in the first two panels of figure 21 [197–199]. Plasmas in this device were formed first as an arc between two circular electrodes. The magnetic fields created by the arc current drives the plasma axially into a ‘flux conserver’ in which the final configuration is obtained [197]. Using the data shown and the device’s nominal minor radius of 0.31 m, the density normalized to the Greenwald scaling law is calculated and plotted in the final panel of the figure. While not following the empirical law precisely, the agreement is surprisingly good. Later data from this experiment show similar agreement [200]. Optimized operation for the device was with average current density of 1–1.5 MA m<sup>-2</sup> and at densities from  $0.5 \times 10^{20}$  to  $1 \times 10^{20}$  [201]. A ratio that would not be out of place in the tokamak or RFP database. Studies of the CTCC-I spheromak, a somewhat smaller device with a  $\sim 0.2$  m and  $I_p(\text{max}) \sim 0.08$  MA, yield a very similar result. At the time of peak fields, the normalized density  $n/n_G \sim 1.2$  and drops to 0.5 about 700  $\mu\text{s}$  later [202]. Similar numbers were reported on the S1 spheromak, where the normalized density ran from 0.5 to 1.5 [203]. Scaling studies however, revealed no marked increase in the operating plasma density with current density. The most recent spheromak work revealed nearly identical results. The SSPX device with an minor radius of about 0.21 m reported line-averaged densities of  $1.6 \times 10^{20}$  with an injection current of 0.2–0.35 MA, i.e. with  $n/n_G \sim 0.6$ –1.1 [204].

Comparison with FRCs is even more difficult. While the basic plasma geometry is toroidal, these devices have quite different magnetic field configurations and shapes. Still, the empirical formulas can be applied and yield a moderate level of agreement. For example, the FRX-C/T device, with minor and major radii of 0.025–0.05 cm (the aspect ratio is of order 1) and a poloidal field of 0.7 T reaches densities of  $(20\text{--}40) \times 10^{20}$  [205, 206]. Using the internal currents that can be inferred from field measurements,  $I/\pi a^2 \sim 20\text{--}40$ . Whether this result is a coincidence or reveals some deeper underlying mechanism is impossible to tell at this time. More recent FRC devices operate roughly in the same range of normalized densities [207, 208].

### 3. Physical mechanisms for the density limit

#### 3.1. Introduction

While empirical scaling provides a reasonable basis for predicting the density limit in new experiments, reliable extrapolation will ultimately depend on an understanding of the underlying physical mechanisms. Such an understanding should unify past observations as well as provide a predictive capability. Experimental results, embodied only in part by the scaling laws, are the ultimate guide and test for theoretical understanding. Though internal details of proposed models may be complex, in the end the result should be as robust with respect to details as the experiments. That is, we should expect the model to find a limit which depends strongly on the poloidal magnetic field strength and is not terribly sensitive to plasma shape or topology, the details of the divertor or limiter, or the nature of wall materials. At the same time, theoretical work on the limit can help to focus experimental investigations, suggesting regimes to study, parameter scans to carry out or important measurements to make.

For the tokamak, there is a generally accepted picture for the density limit which involves edge cooling, current profile shrinkage followed by the loss of MHD equilibrium [108]. In the stellarator, with no plasma current, the limit apparently involves only the first step and is manifested by a loss of thermal equilibrium. In tokamaks, the phenomenology of the density limit, loss of global confinement, H/L transitions, MARFEs, poloidal detachment, and

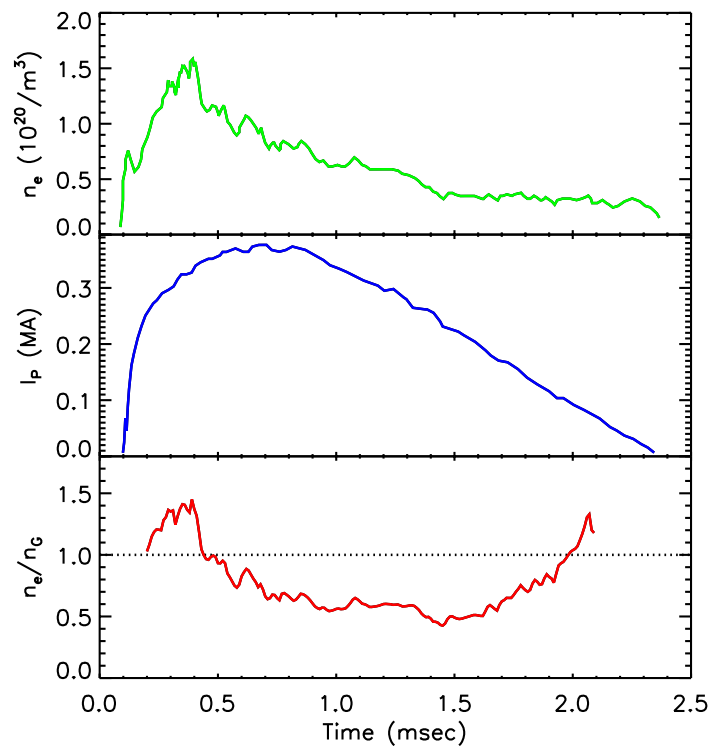


**Figure 21.** Traces of density, plasma current and normalized density from the CTX spheromak are plotted. These experiments were not aimed toward the study of density limits, rather they were the result of discharge optimization through the variation in gas fill pressure. It is not clear if the near coincidence of the normalized density with the tokamak and RFP scaling laws is the result of common physics [199].

divertor detachment are associated with cooling of the edge plasma. All occur in roughly the same part of parameter space, suggesting a unifying mechanism. The overarching questions are, ‘what is the physics that causes the edge cooling?’ and ‘why does it cause the density limit in a particular part of parameter space?’ A comprehensive and predictive theory should also identify critical local variables and be capable of relating these to global or engineering variables. The challenge is to meld the diverse and complex physics into a theory with simple and robust predictions.

Proposed theories can be categorized on the basis of the part of the plasma they focus on and which physical mechanisms they emphasize. Most work has concentrated on the edge plasma, though studies on the limit in stellarators have continued to look at core physics [209, 210]. At the edge, theories have investigated plasma both inside and outside the separatrix. In the separatrix, one can emphasize the plasma immediately surrounding the core or that in the divertor. The physical mechanisms studied have included the effects of neutrals, radiation and transport on radial power balance as well as parallel power balance along open field lines and its effect on the divertor equilibrium. In a real plasma of course, these effects cannot be entirely decoupled. For example, power and particle fluxes are coupled to profiles through the transport mechanisms. These profiles also determine the rates for radiation, ionization, charge-exchange and other atomic physics effects which cannot be ignored in the plasma edge. Theories which attempt to compute the density limit in the SOL or at the separatrix typically need a separate theory for extrapolating to the core density.

### 3.2. Radiative collapse and thermal stability

Theoretical considerations of the thermal stability of a current carrying plasma column [211, 19] and experimental observations which associated disruptive plasmas with high levels of impurities led investigators to these mechanisms for the density limit [19, 212–217]. Several scenarios have been considered. In the first, radiation from high  $Z$  impurities in the plasma core leads to cooling across the entire profile and to a discharge quench. In the second scenario, impurity radiation leads to a thermal condensation in the plasma edge by competing effectively with heat transport. The appearance of these condensations, or MARFEs, have been shown to scale in the same manner as the density limit [34, 66]. A third scenario involves the radial contraction of the temperature profile due to the competition between radiation and perpendicular heat conduction near the plasma boundary. Finally, a density limit can be derived by considering the impact of radiative heat loss on the pressure profile and MHD stability [218]. A common thread for all scenarios is the increase in radiated power with density,  $P_{\text{rad}} = n_e n_Z R(T)$ , where  $R(T)$  is the radiative cooling rate and depends only on the electron temperature and the atomic physics of the impurity ion. For a constant impurity fraction ( $Z_{\text{eff}} = \text{constant}$ ),  $P_{\text{rad}}$  increases as the square of the density for a given temperature. The manifestation of these mechanisms depends, to an extent, on the type of confinement device under consideration. The critical point is that they may cause the plasma to cool dramatically leading to the wide range of phenomenology described earlier.

#### 3.2.1. Core radiation

The Murakami limit was suggested by the relation between the Ohmic heating rate and core radiation from moderate and high  $Z$  impurities [20]. The heating rate is proportional to the central plasma current density which scales as  $B/R$  in a sawtooth discharge. While details of the disruptive process were not worked out, it was clear that for sufficient concentrations of high  $Z$  impurities, strong central cooling could lead to current profiles which were grossly unstable to MHD modes. While this mechanism is generally not responsible for the density

limit in tokamaks under most circumstances, in cases where core transport is reduced and/or a strong inward pinch is present, central impurity levels can build up and lead to a discharge quench or to MHD instability. There is evidence that bulk radiation is important for the limit in stellarators. Experiments in W7-AS found a ‘soft’ density limit that was associated with high levels of core radiation [191]. The subsequent quench occurs on an energy confinement timescale. Using the global energy confinement scaling to evaluate the conducted power and balancing it against radiation, an expression for the density limit was obtained which roughly matched the empirical expression for stellarators. A more general treatment yielded similar results,  $n \propto P^{1/2} B^{1/2} V^{-1/3} q^{-1/4}$  [209]. The magnetic field scaling in this relation comes entirely from the assumed transport law. The power scaling and the overall coefficient for the limit depends on the density and impurity profiles as well as the cooling curves for the particular impurities present. Similar results have been obtained in analysis of RFP density limits [26]. A density limit proportional to the plasma current density was found when radiation in the current carrying channel exceeded input power from Ohmic heating [177].

Another approach to the stellarator density limit problem included the important contribution of ergodic field lines to transport in the boundary region [210]. In this paper, the energy balance equation is solved by dimensional analysis leading to an expression for thermal conductivity driven by resistive ballooning turbulence constrained by experimental observations. Including radiation, a bifurcated solution is found which includes stable low- and high-temperature branches. Transitions from the high temperature to low temperature solution are interpreted as the density limit. Since in a stellarator, feedback through the current profile can’t occur, MHD equilibrium is not lost and the plasma simply decays on an energy confinement time. With some simplified modelling of impurity radiation, expressions for the density limit were obtained which depend on the choice of transport models. Transport driven by  $(\tilde{T}_e \tilde{B})$  correlation were shown to give rise to gyro-Bohm-type scaling. Under these conditions the critical density for bifurcation was

$$n_{\text{limit}} \propto \frac{P^{0.69} B^{0.75} t^{0.37}}{(Ra^2)^{0.31}} \quad (3.1)$$

which is qualitatively in agreement with experimental results from W7-AS [191]. The formalism did not allow a single simple scaling law to be obtained which was valid for all cases. The radial location of the bifurcation is not fixed at any point on the profile, but may vary according to the particular choices of magnetic field, impurity profiles and transport model.

### 3.2.2. Stability against radiative condensation—MARFE formation

The simplest models for MARFE formation involve only radiation, parallel conduction and a heat source from perpendicular transport [219–223]. A thermal collapse or condensation can occur at temperatures where the cooling rate,  $R(T)$ , decreases strongly with temperature. Thus, a negative temperature perturbation leads to more radiation and still lower temperatures. Pressure conservation results in a positive density perturbation which also contributes to increased radiation. Following the approach of [223] and using the geometry as defined in figure 22, the stability of a radiating region of density  $n_m$ , temperature  $T_m$  and length  $L_m$  at the end of a flux tube of length  $L$ , density  $n$  and temperature  $T$  can be considered. Balancing power conducted down the flux tube to radiation yields

$$\frac{4 \kappa_0 (T_0^{7/2} - T_m^{7/2})}{7 L} = \alpha_Z n_m^2 R_Z(T_m) L_m \quad (3.2)$$

where  $\alpha_Z$  is the impurity fraction,  $n_Z/n_e$ , and  $\kappa_0$  is the coefficient for classical heat conduction. Using pressure balance  $n_0 T_0 = n_m T_m$  (which ignores friction with neutrals and recombination)

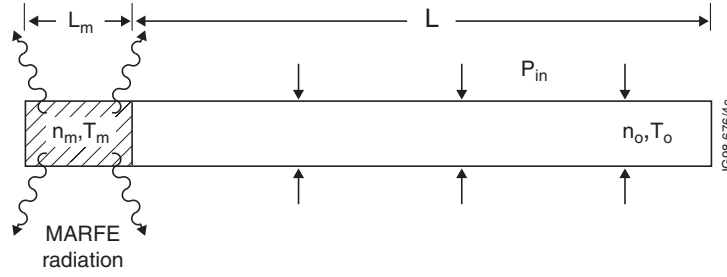


**Figure 22.** The geometry for a simple radiative condensation (MARFE) model. A flux tube of length  $L$  has a high temperature  $T_0$  at one end and a low temperature  $T_M$  at the other. With  $T_0 \gg T_M$ , pressure balance requires  $n_0 \ll n_M$ . Strong radiation driven by the high densities and low temperatures at the cold end together with reduced parallel thermal conductivity sustains the temperature gradient [223].

and assuming  $T_0^{7/2} \gg T_m^{7/2}$ , which is applicable in the strongly radiating regime, equation (3.2) becomes

$$\frac{R_Z(T_m)}{T_m^2} = \frac{4\kappa_0}{7\alpha_Z f_m} \frac{T_0^{3/2}}{L^2 n_0^2} \quad (3.3)$$

where  $f_m = L_m/L$ . The left-hand side of this equation has a maximum at temperatures of a few eV for low  $Z$  impurities. Stability against radiative collapse requires that the right-hand side exceed this maximum, excluding the MARFE solution to the heat balance equation. This will clearly be possible below some critical density,  $n_c$ , which can be calculated from (3.3).

$$n_c = \left[ \frac{4\kappa_0 T_0^{3/2}}{7\alpha_Z f_m L^2 \{R_Z/T^2\}_{\max}} \right]^{1/2} \quad (3.4)$$

Using  $L = \pi q R$  as an approximation for the length of the flux tube, yields

$$n_c = \frac{I_p}{\pi a^2} \frac{1}{B_T} \left[ \frac{\mu_0 \kappa_0 T_0^{3/2}}{7\pi^2 \alpha_Z f_m L^2 \{R_Z/T^2\}_{\max}} \right]^{1/2} \quad (3.5)$$

Thus, in this highly simplified model, a threshold for MARFE formation is found which scales with the empirical density limit. In this expression,  $I_p/a^2$  comes from the connection length of the flux tube. The derivation which led to equation (3.5) ignores a good deal of important physics including perpendicular heat transport, parallel convection and neutral effects. While suggestive, it differs from the experimental observations of the density limit in important ways. Including the effects of perpendicular transport does not change the basic picture of MARFEs but can affect aspects of their formation, including poloidal symmetry and threshold [221]. In the heat balance, both perpendicular and parallel conduction are stabilizing while density and impurity fraction are destabilizing. Stability is greater in the presence of a large perpendicular temperature gradient which leads to a narrower radiating layer [224]. One might expect that convective losses, which do not require the presence of strong temperature gradients for a given heat flux, would not be as stabilizing and could more readily lead to MARFE formation. In two-dimensional simulations, the thermal instabilities appear as MHD eigenmodes and confirm the analytic results [225]. MARFEs are found at a fraction of the density limit, typically 0.4–0.7 $n_G$ . The localization of the MARFE on the low-field side of the torus is explained, in this case, by effects of toroidicity and MHD stability rather than through an asymmetric heat source. An expression for MARFE stability in terms of global variables has been derived from the local

stability equations by using the L-mode scaling law to eliminate temperature and employing a simple fit to the radiation curves [143, 46]. This exercise yields weaker  $B_T$  dependence than equation (3.5):

$$n_c \propto \frac{I_P^{0.96}}{a^{1.9}} \alpha_Z P_{\text{in}}^{0.43} R^{0.17} B^{0.04} (\kappa^2 (1 + \kappa^2))^{0.22} \quad (3.6)$$

where  $\kappa$  is the plasma elongation. While the applicability of global scaling laws to the plasma boundary and assumptions which relate local to average density are somewhat questionable, the result is intriguingly close to the empirical expression for  $n_G$ .

The discussion above refers mainly to dynamics in the main chamber, typically near the midplane of limiter plasmas. Similar analysis has been carried out for the SOL of divertor plasmas [226, 227]. This approach has similarities to the analysis of divertor detachment which will be discussed in section 3.3, but does not consider momentum loss to neutrals and thus does not capture the essential detachment physics. A density limit is found in the sense that the solution to the energy balance equations in divertor geometry yields a maximum separatrix density as a function of the divertor sheath temperature (or input power). Assuming a power law form yields

$$n_c \propto \frac{q_{\perp}^x B^{0.31}}{(qR)^{0.69-x}} \quad (3.7)$$

where  $q_{\perp}$  is the average perpendicular heat flux into the radiating flux tube. In this equation,  $x$  is an undetermined parameter.

### 3.2.3. Radial detachment and stability of radiating layer

Depending on the balance between perpendicular heat transport and radiation, a radiating layer at the edge of a plasma may be stable and stationary, or may propagate inward, shrinking the temperature profile leading to MHD unstable current or pressure profiles. The edge safety factor will decrease as the radius of the current channel is squared. This can rapidly lead to a current driven instability which appears near  $q = 2$ . The problem is approached by considering the stability of the energy balance equation to temperature perturbations [213–216, 221, 228, 57, 229–232].

The simplest models assume the density at which the plasma ‘detaches’ from the wall is where radiation removes all of the conducted power. The net power to the wall can be calculated by integrating the heat balance equation

$$Q_{\text{plasma}}^2 - Q_{\text{edge}}^2 = 2n_e n_Z \kappa \int_0^{\infty} dT R(T) \quad (3.8)$$

where  $Q_{\text{plasma}}$  is the heat flux from the core plasma to the radiating layer and  $Q_{\text{edge}}$  is the heat flux from the layer to the wall. The plasma detaches thermally when  $Q_{\text{edge}} = 0$ , leaving

$$Q_{\text{plasma}} \propto (n_e n_Z)^{1/2} \quad \text{thus} \quad n_c \propto \frac{P}{(Z_{\text{eff}} - 1)^{1/2}} \quad (3.9)$$

If this radial thermal detachment is associated with the density limit, it would scale strongly with input power and tend to diverge as  $Z_{\text{eff}} \rightarrow 1$ . The model can be carried forward using Ohmic heating for the heat source and eliminating the temperature dependence by a particular choice of global transport models to obtain a relation which is not too different from the Hugill or Greenwald limits [216, 231]. However, this is not a general result. Use of other (perhaps more appropriate) transport models leads to very different expressions [214, 112]. To determine whether the thermal detachment is stable or leads to radial contraction, the heat balance equation can be linearized about an equilibrium solution with a thin radiating layer

near the boundary at  $r = a_p$  using Ohmic heating and Spitzer resistivity. The stability criterion becomes [231]

$$-\frac{a_p}{n} \frac{dn}{da_p} > \frac{3}{2} \quad (3.10)$$

The essential effect in this model is the increase in radiation which occurs as the plasma shrinks into regions of higher density. The derivation that led to equation (3.10) assumed that the input power and density profile do not change appreciably during the contraction. Using data from experiments with  $P_{\text{rad}} \sim P_{\text{in}}$ , it is found that (3.10) is not difficult to satisfy, i.e. only in special circumstances does the plasma detach stably. However, as discussed, many experiments report reaching the density limit with far less than 100% power. In this case, it can become difficult to satisfy (3.10). This constraint can be eased by consideration of more realistic boundary conditions [232]. In this case, radial detachment can occur for  $P_{\text{rad}}$  at only a fraction of  $P_{\text{in}}$ , even in the case of flat density profiles. A complete treatment needs to include realistic models for plasma heating, transport and the details of impurity radiation [230] resulting in coupled nonlinear equations that must be solved numerically. Such calculations can recover a good deal of the density limit phenomenology [233]. Radial thermal instability tends to dominate with high concentrations of impurities, while divertor detachment dominates for lower concentrations. At very high current densities, neutral penetration can lead to fuelling limits. So far these models have used only very simple models for energy transport and have not included convected heat loss or particle transport.

### 3.3. Role of divertor equilibrium and detachment

A good deal of recent work on radiation models of the density limit has focussed on mechanisms associated with divertor detachment. This work is motivated by the observation that at least on some machines, detachment occurs just below the density limit [9, 84]. The basic approach is to solve the two-dimensional divertor problem, typically with a two point model [234–236, 223] or by numerical modelling [84, 237] and then to look for bifurcations or loss of solution at high density. In these models, anomalous perpendicular heat flux balances classical parallel electron heat transport. As the core and upstream densities are raised, the upstream temperatures drop through pressure balance. The downstream temperature drops much more quickly since the parallel heat conductivity scales as  $T_e^{5/2}$ . Radiation increases, driving the divertor temperature still lower. Thus far the scenario is similar to that for MARFE formation. However, detachment is not simply a radiative condensation. Starved for power, the plasma in front of the divertor plates can reach the point (typically about 5 eV) where interactions with neutrals serve as a momentum sink to plasma flowing to the divertor after which particle, momentum and energy fluxes to the divertor drop nearly to zero. At this point, recombination sets in further reducing plasma contact with the material surface. A low temperature is therefore, a necessary but not a sufficient condition for detachment since divertor detachment would not occur without significant neutral interaction. Calculation of the detachment threshold leads to a critical separatrix density,  $n_{\text{sep}}$ , which then must be related to the core density. In the absence of credible models for particle transport, the usual assumption is to pick a ratio of  $\bar{n}_e$  to  $n_{\text{sep}}$  guided by experimental results [84].

Details of detachment threshold calculations are quite involved and can be found in the references. Here, the approach will be discussed and the main results summarized. The computation volume includes a narrow flux tube of length  $L \sim qR$  which runs from the ‘upstream’ stagnation point to a gas target which is at some distance from the divertor plates. The details of the gas target are not treated analytically (though they are included in numerical

computations). The width of the flux tube is approximately a power scrape-off distance. The essential equations are particle, momentum and energy balance. The introduction of a momentum loss term for the plasma ions limits particle flux and upstream plasma density as a function of power flux (or temperature) which would otherwise increase indefinitely as the power was lowered. Above this maximum density point, no solution to the equations exists. It is assumed that this detachment point is associated with the density limit. The expression for the maximum separatrix density can be simplified by assuming a power law form (and introducing an undetermined constant,  $\beta$ ) yielding an expression [236]

$$n_{\text{sep}} \propto \frac{q_{\perp}^x B^{5/16}}{(qR)^{11/16-x}} \quad \text{where } x = \frac{10 - \beta}{16(1 + \beta)} \quad (3.11)$$

To be compatible with experimental data, the arbitrary constant,  $\beta$ , must be greater than 1.5, which is true only for an ‘intermediate’ neutral collisionality regime. While it is not clear that all experiments which follow the empirical scaling law operate in this regime, there is evidence that this equation provides a good fit to experimental data on ASDEX Upgrade [105], and JET [84, 238]. Figure 23 shows a successful comparison between JET data and the SOL model. Discrepancies have also been reported. In DIII-D, the separatrix density is found to scale in accordance to this model, but not the separatrix temperature [46, 47]. The absolute value of separatrix density does not agree with the model unless very strong perpendicular transport ( $\sim 100$  Bohm) is assumed. In these experiments (and others as discussed above), core plasma densities well above the detachment threshold have been reported. Typically, the detachment threshold density scales as a much stronger function of power than the density limit [73, 239]. Two-dimensional divertor computations have yielded reasonable agreement with experimental data [237] with divertor detachment found to occur over a wide range in density. Extending these results to the core plasma density limit required an assumption for the ratio of SOL to core density. Interestingly, these simulations found no clear limit in pure hydrogen plasmas, emphasizing the role of impurity radiation even in regimes where neutral dynamics are believed to dominate.

Despite the complexity of the physics, the terms in equation (3.11) have a fairly straightforward origin. The  $B$  scaling comes entirely from an assumption of Bohm scaling for the perpendicular transport. It enters because any decrease in transport (at higher field, for example) also decreases the width of the SOL and thus increases the parallel power flux density.

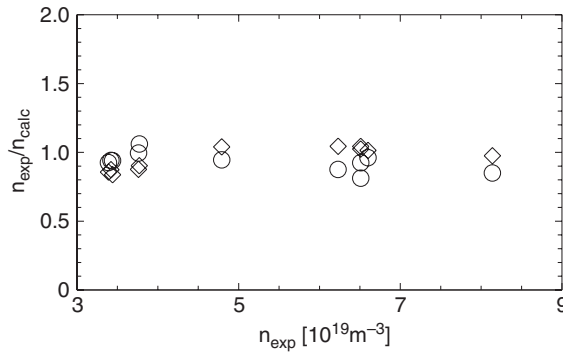


**Figure 23.** A comparison of data from JET with the results of a divertor scrape-off model and the Greenwald scaling. Open circles indicate points normalized to the empirical scaling and diamonds indicate points normalized to the model. The experimental data cover the range  $2.3 \text{ MW} \leq P_{\text{in}} \leq 12.5 \text{ MW}$ ,  $2.4 \leq q_{\varphi} \leq 4.0$ ,  $1.0 \text{ T} \leq B_{\text{T}} \leq 2.5 \text{ T}$  [84].

Agreement with the experiments limits the choices for the transport law. Note, however, that there is strong evidence on at least some machines that the perpendicular transport in the SOL does not scale with  $B$  [240, 241, 54]. In this case, a density limit would be derived which did not resemble the experimental results. The second important component of the equation is a power of the parallel connection length. It shows up in the denominator (recall that a power law form has been imposed) since an increase in the connection length assists the thermal decoupling of the upstream and downstream plasmas.

A similar mechanism has been proposed to explain density limits in stellarators. The fraction of radiated power to input power at the density limit was substantially less than one in W7-AS, suggesting that any power balance problem was local rather than global [8]. Rough agreement with SOL model was observed, though no divertor instability was detected with the diagnostics available at the time. More recent results included measurements of the edge temperature and density and found a maximum in the edge density which occurred just before the discharge collapsed [242, 243].

### 3.4. The role of transport

#### 3.4.1. Introduction

While radiation models have had some success in explaining experimental results, they have shortcomings which suggest that they are incomplete at best. The various models seek to identify the density limit with  $P_{\text{rad}}/P_{\text{in}} \sim 1.0$ , MARFE formation, poloidal detachment, or divertor detachment. These phenomena all exhibit density threshold behaviour, but experimental thresholds can range as low as a quarter of the ultimate density limit (see table 1 and references therein). Moreover, these models generally predict strong sensitivity to power input and impurity content and often to details of divertor or limiter geometry. They depend on models for heat and particle transport which do not necessarily match experimental observations. The overarching question is whether radiation related phenomena are a cause of the density limit or a common symptom of some other physics which drives edge cooling—namely density-dependent transport. In other words, is there a maximum density independent of atomic processes? The answer to this question, which may not be the same for every type of confinement device, has important implications for fusion reactor design.

Transport enters the density limit problem in various ways. Radiation models are sensitive to a lesser or greater degree on the choice of transport model used. Improved core particle transport can lead to peaked density profiles and thus higher line-averaged density limits and edge particle transport can enter through the ratio of the average density to the density in the radiation zone. The issue raised here is more basic—does edge transport increase in some critical way as the density is raised and is this increase the fundamental driver for the limit?

#### 3.4.2. Experimental evidence

The incompleteness or inability of the radiation models to explain certain aspects of the experimental results provides the first evidence for the role of transport in the density limit. As discussed in sections 2.2 and 3.2, the appearance of MARFEs, radial detachment, and divertor detachment occur over a wide range in  $n/n_G$ . On the other hand, the near coincidence of the L-mode disruptive limit and the H/L transition limit suggests a common mechanism. Further, density limit disruptions have been observed without any evidence for a (prior) thermal collapse [124, 244] leading to the speculation that deterioration in edge transport may be partially responsible. Radiation models predict a strong increase in the density limit with input power and an equally strong decrease with impurity levels. Numerical studies of a comprehensive radiative model have found that the limit can respond strongly to impurity

content [233]. For moderate  $Z$  impurities, the predicted limit increased a factor of 3 from  $0.6n_G$  to  $1.8n_G$  as  $Z_{\text{eff}}$  was dropped from 1.6 to 1.0. There is no experimental evidence for such behaviour. Experiments on the ETA-BETA II and RFX RFPs suggested that the limit in RFPs is not necessarily a radiation limit [176, 13]. Local power balance analysis using recent bolometric measurements finds that radiation doesn't play an important role at any radius [186]. In contrast, the explosive growth of the L/H power threshold which is seen near the density limit [41, 32] and the sharp drop in edge pressure [50] suggest a transport catastrophe. This suggestion is amplified by studies of the edge operating space boundaries for various H-mode regimes [245, 91]. A drop in the edge temperature gradient was observed and interpreted as an increase in edge cross-field transport and was correlated to collisionality. Curves of constant collisionality were also found to be correlated to the type III ELM and detachment boundaries. Overall, the data were consistent with a model for the density limit based on collisionality driven transport.

Direct evidence for the role of convective losses as a cause for the density limit was first reported in observations of an anomalous drop in particle confinement seen for pellet fuelled discharges in Alcator C [3]. In these experiments, similarly sized deuterium pellets were injected into discharges with different values of plasma current. For densities well below  $n_G$ , the particle decay time was similar to the energy confinement time, about 0.05 s. As densities approached and exceeded the limit, the decay time dropped by about an order of magnitude. Similar experiments on DIII-D found a decay which depended on  $I_P$  rather than  $I_P/n_e$  [144]. In contrast, ASDEX has reported no change in global energy or particle confinement for discharges gas fuelled to the density limit [9]. A series of experiments on the MTX device measured particle transport by perturbative means [246]. Using a modulated gas puff and the resulting time-dependent density profiles, profiles of the particle diffusivity,  $D$ , and convective velocity,  $V$ , were obtained (figure 24). A large increase in both  $D$  and  $V$  were found as the density limit was approached while the edge temperature and gradient dropped precipitously. Similar results were obtained on TEXT, which used the propagation of sawtooth perturbations to probe thermal and particle diffusivities as a function of plasma density [247]. Both  $\chi_e$  and  $D$  increased strongly as the density was raised, even well before a density limit disruption. The change in transport was correlated with a significant increase in low-frequency fluctuations with moderately high wave numbers,  $k_\theta \sim 12 \text{ cm}^{-1}$  corresponding to  $k\rho_s \sim 0.3\text{--}0.9$ . Spatial resolution in these experiments was not sufficient to localize the

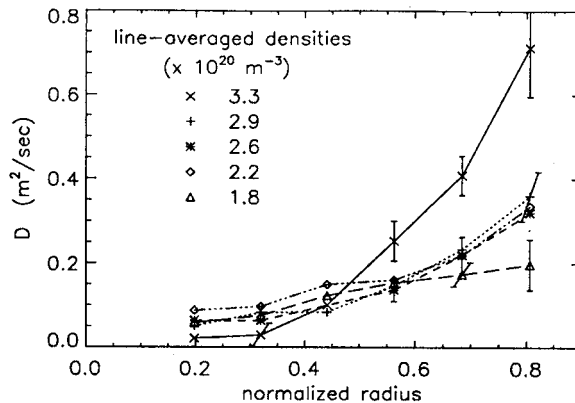


**Figure 24.** Profiles of diffusion coefficients calculated from modulated gas puff experiments on the MTX tokamak. As the density limit is approached, the edge diffusivity increases [246].

source of the fluctuations.

Detailed measurements of edge profiles and fluctuations from C-Mod provided some new insights into the role of cross-field transport in the density limit [54]. Measurements with a fast scanning electrostatic probe found two distinguishable regions in the SOL. Near the separatrix, density and temperature profiles were steep, with gradient lengths of the order of 5 mm or shorter. The fluctuations in this region were of moderate amplitude, with autocorrelation times on the order of  $1 \mu\text{s}$ . Using a high-resolution Lyman  $\alpha$  array to determine the ionization source, the particle transport could be calculated and convective losses estimated. The effective diffusivity,  $D_{\text{eff}} = \Gamma / \nabla n$  was found to scale with the parallel collisionality as  $(L/\lambda_{ei})^{1.7}$ , where  $\Gamma$  is the integrated particle source and  $\lambda_{ei}$  is the mean free path for electron–ion collisions. Flows down the open field lines to the divertor were found to be an unimportant component of the particle balance. Beyond this region, in the far SOL, profiles were much flatter and fluctuations were large and bursty. The autocorrelation time for fluctuations in this region was of the order of  $20\text{--}40 \mu\text{s}$ . The far SOL region had very large cross-field transport, well in excess of parallel losses for both particles and energy. As the density was raised, the breakpoint between the two regions move inward toward the separatrix. Figure 25 shows a set of data from these experiments, demonstrating the profiles and trends at low density. Figure 26 shows the relationship between parallel and perpendicular losses for these discharges. The domination of perpendicular transport over parallel conductivity as the density is raised is clear. As the density limit is approached, the regime of strong cross-field transport crossed the separatrix and intruded into the core plasma. Figure 27 shows the plasma profiles, fluctuation levels, and autocorrelation times during this process. The gross features of SOL profiles discussed above are not new or unique to C-Mod. TEXT [248], ASDEX [249], T10 [250], DIII-D [251] and

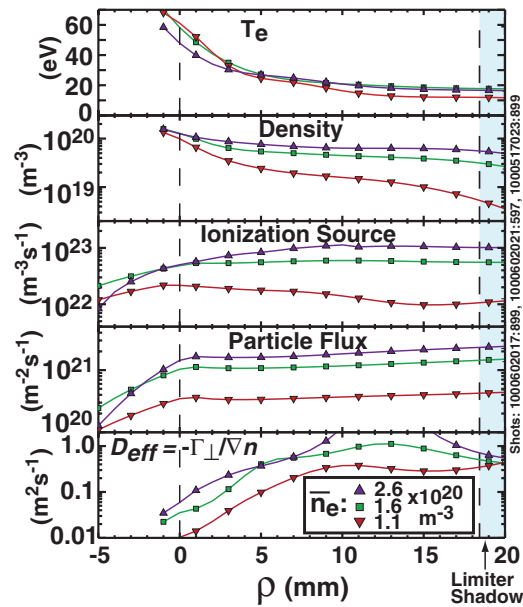


**Figure 25.** Profiles from the SOL in the C-Mod tokamak. Two regimes are evident from the temperature profile—a region of low cross-field transport and large gradients near the separatrix and a region of high transport and small gradients in the far SOL. As the density is increased, the region of high diffusivity extends inward [54].

JT60-U [252, 70] have reported SOL profiles with two distinct regions. The W7-AS stellarator found similar results [253, 254]. Data from a fast reciprocating probe showed a strong increase in fluctuations in the far SOL [255]. On ASDEX, a clear increase in correlation time and length were seen at higher densities [256]. An increase in turbulence driven flux with density was seen on JET [250].

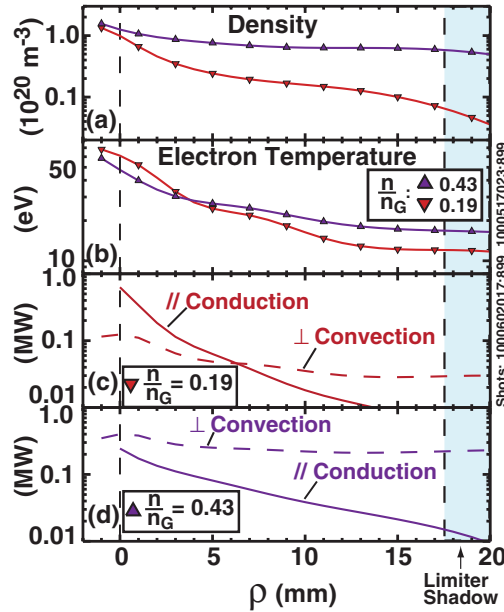


**Figure 26.** A comparison of parallel conductive losses and perpendicular convective heat loss in the C-Mod edge. As the density is raised, cross-field transport begins to exceed parallel transport [54].

These observations provide the ingredients for a density limit based on edge transport. The temperature profile in the SOL divides into two regions as a result of the relative competition between parallel heat transport, which scales as  $T_e^{7/2}$ , and perpendicular losses, scaling through the collisionality, as an inverse power of the temperature. The break in the profiles divides the parallel transport dominated near SOL from the perpendicular transport dominated far SOL. The positive temperature scaling for parallel conductivity is stabilizing in the sense that negative perturbations in temperature lead to drastically reduced heat loss. Positive perturbations strongly increase the heat loss; perturbations are damped in either case. As the density increases, the corresponding drop in temperature shifts the balance toward cross-field losses. Unlike the parallel losses, the collisionality scaling of the perpendicular transport is unstable. Lower temperatures lead to higher collisionality, higher transport and thus still lower temperatures. The inward movement of the low-temperature regime can then lead directly to the progression of phenomenology that is observed as the density is raised toward the limit. Divertor detachment naturally occurs, since perpendicular losses starve the divertor of the power that is needed to support attachment. H-mode confinement, which is dependent on a hot edge boundary condition, drops and eventually the plasma reverts to L-mode. As the density is raised still higher and without the thermostatic effect of parallel transport, the core plasma is eroded and the current and pressure profiles shrink, leading to MHD instability. An essential requirement for this hypothesis is a systematic increase in transport at higher densities or collisionalities. Theories for density-dependent transport will

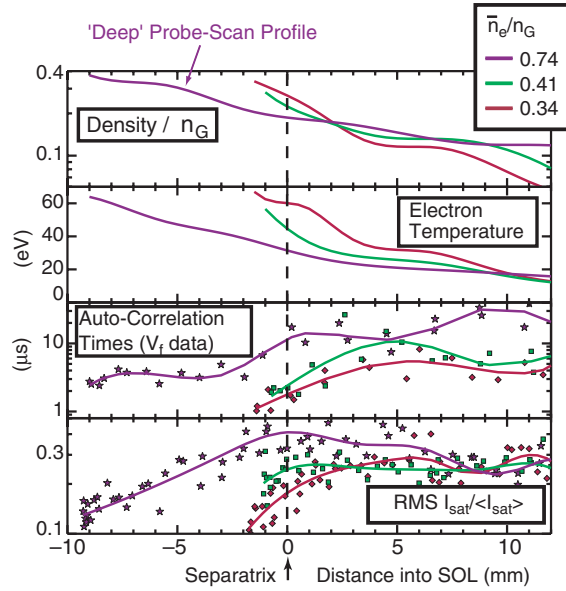


**Figure 27.** Edge profiles from C-Mod as the density limit is approached. The regime of strong transport with large, long-correlation time fluctuations moves across the separatrix and into the main plasma.

be discussed in the next section.

### 3.4.3. Theoretical support

A number of models have been proposed to explain an increase in transport at high densities and its relation to the density limit. Most are based on detailed calculations of specific micro-instability mechanisms or numerical modelling; others have considered the role of neo-classical transport [257] or have taken a more phenomenological approach. The understanding of transport and turbulence in the plasma edge has proven to be a particularly difficult problem. While experiments have found very high levels of fluctuations and transport, linear calculations tend to find that most modes are stable [189]. In any event, generic drive mechanisms like pressure gradients, curvature or current gradients are not affected directly by the plasma density. Instead, the proposed mechanisms work through dissipation terms, relying on the lower temperatures which are produced as the density is raised. As the temperature is lowered, resistive ballooning and resistive gradient modes, which rely on finite conductivity, are more unstable [258]. Nonlinear calculations of the resistive gradient instability found a significant increase in fluctuation levels and turbulent transport [258]. Inclusion of additional radiation physics led to a possible explanation for the observation that potential fluctuations  $e\tilde{\phi}/kT$  are as large as  $\tilde{n}/n$  in the plasma edge. Without this addition, the potential fluctuations were much smaller than what had been measured in experiments. An analytic and numerical approach for the nonlinear stability of drift waves found a significant increase in the turbulence levels at high density. A critical density of the form  $n_{\text{crit}} \propto \varepsilon B/qR$  was found [259]. The turbulence causes strong electron cooling scaling with the collisionality,  $\chi_e \propto n^{1/3}/T^{5/6}$ , which can lead to a thermal collapse. With inclusion of atomic physics this approach led to a power dependence of the form  $n_{\text{crit}} \sim P^{1/2}$  [260].

Proper modelling of turbulence in the plasma edge must include full treatment of

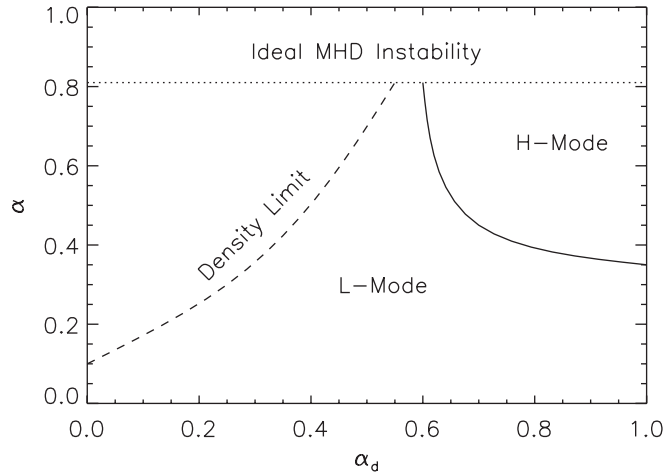


**Figure 28.** A phase space diagram for edge turbulence derived from a set of electromagnetic gyro-fluid simulations. The axes,  $\alpha$ , the normalized pressure gradient and  $\alpha_d$ , the diamagnetic parameter are defined in the text. The density limit boundary was characterized by extremely high levels of turbulence and transport, typically orders of magnitude above L-mode. This region corresponds to high collisionality [266].

parallel electron dynamics, electromagnetic and diamagnetic effects [261–264]. The resulting turbulence is an amalgam of drift, Alfvén and ballooning waves and often referred to as drift-Alfvén or drift-ballooning turbulence. Three-dimensional nonlinear gyro-fluid simulations, which include the appropriate electron dynamics and diamagnetic effects, have found a region of exceptionally high transport which may model density limited discharges [265, 266]. The results are summarized as a ‘phase space’ diagram in figure 28, The axes of this diagram are the normalized pressure gradient,  $\alpha = -Rq^2 d\beta/dr$ , and the diamagnetic parameter,  $\alpha_d = \rho_s c_s t_0 / L_n L_0$  where,  $c_s = \sqrt{(T_e + T_i)/m_i}$ ,  $t_0 = (RL_n/2)^{1/2}/c_s$ ,  $\rho_s = c_s/\Omega_i$ ,  $L_0 = 2\pi q (v_{ei} R \rho_s / 2\Omega_e)^{1/2}$  and  $L_n$  is the density scale length. Simulations just inside the boundary marked ‘density limit’ have very high levels of turbulence and transport; deeper into this region the simulations don’t converge. The effects at low values of  $\alpha_d$  come from the nonlinear development of resistive ballooning modes. Transport at higher  $\alpha$  is due to the dependence of the turbulence saturation level on magnetic perturbations. Using the parametric dependence of  $\alpha_d \propto \sqrt{T^3/n}$  and  $\alpha \propto q^2 n T / B^2$ , it is apparent that the portion of parameter space in question is consistent with low-temperature and high-density regimes, which are typical near the density limit. In this picture, the poloidal field may enter through the  $q/B$  dependence of the MHD  $\alpha$  parameter. Figure 29 shows data taken from ASDEX Upgrade just below the density limit, plotted in the  $\alpha$ – $\alpha_d$  plane. Using typical ASDEX Upgrade parameters  $R = 1.65$  m,  $a = 0.5$  m,  $B = 2.5$  T,  $T_e = 50$  eV,  $n = 0.3e20$ ,  $Z_{\text{eff}} = 2$ ,  $q = 4$ ,  $\alpha_d = 0.3$ ,  $\alpha = 0.5$ ,  $d$  calculated from simulation is of the order  $60 \text{ m}^2 \text{ s}^{-1}$ . Transport at that level would almost certainly lead to a collapse of the edge plasma. A source of the plasma current scaling has been proposed based on the competition between collisionality driven transport and the stabilizing effects of  $E \times B$  shear flow [267]. In this model, the critical element in the density limit progression is the destruction of the edge shear layer. So far, the simulations have been carried out in flux tube geometry with local profiles; background parameters and their gradients are constant across the computational volume. The effects of X-point geometry and real profiles have not yet been assessed. The effects of diminishing FLR effects at high

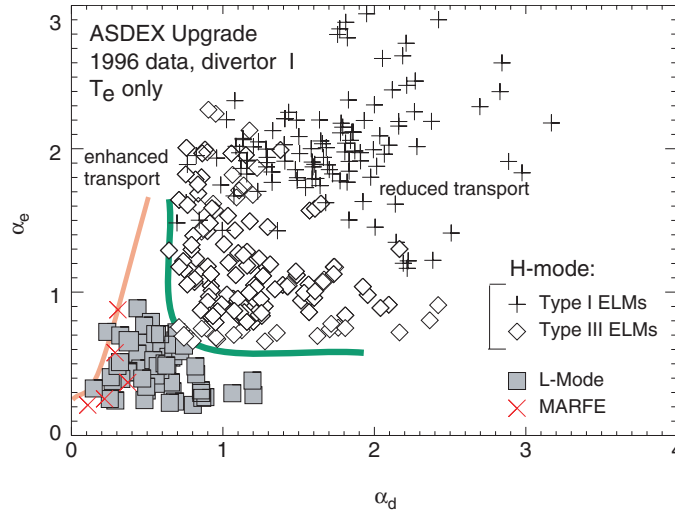


**Figure 29.** A comparison of edge data from ASDEX Upgrade with the curves shown in figure 28. Discharges near the density limit, indicated by the symbol X, roughly map out the theoretical boundary [245].

density have also been studied in the context of MHD theory [268]. In this paper, a density limit is found which corresponds to the growth of ballooning modes through the loss of FLR stabilization. The role of sheath physics on turbulence on open field lines has been recently addressed [269]. In these studies, large coherent structures ('blobs') undergo  $\nabla B$  polarization and drift rapidly across the SOL under the influence of the  $E \times B$  drift.

Several authors have taken a more phenomenological approach to this problem. Using aspects of the transport equations which are related to the poloidal resistivity, underlying symmetries in the particle, thermal and magnetic diffusivity have been exploited [270]. Combined with source terms and boundary conditions, which were consistent with experiments, a critical density for electron thermal transport was found. This scaling for  $n_{\text{crit}}$  was proportional to  $I_p^{6/5}$  for Ohmic discharges and  $I_p^{10/9}$  for auxiliary heating. The results are qualitatively in agreement with discharges from the DITE tokamak and close to the empirical results [271]. The expression of physics equations in dimensionless parameters has been employed to explain and interpret various aspects of edge physics [156]. Because of the low temperatures involved, pressure drive was assumed to be unimportant (a questionable presumption in light of recent simulations of edge turbulence [262–264]). In place of  $\beta$ , the normalized collisionless skin time,  $\omega_{\text{skin}}/\omega_{\text{transit}} \propto v^* \rho^*/\beta \propto 1/aT^2$ , was introduced as the third dimensionless parameter. The physical effect was to limit the fluctuation scale and thus turbulent diffusivity. A bifurcation was found which corresponded to the onset of strong skin effects and led to a maximum in diffusivity. This point was interpreted as the L/H transition. This expression for the transition, along with the assumptions that the H-mode pressure gradient is set by ideal ballooning, and the type I to type III boundary is determined by collisionality, yield a maximum operating density for H-modes [272]. Note that this paper also assumed  $k\rho_s \approx 0.2$  and a mixing length approximation for perpendicular diffusion,  $D_{\perp} \propto c_s \rho_s$ . The result is Bohm-like transport and is not necessarily consistent with experimental measurements [240, 241, 54].

### 3.5. Role of neutrals

Neutrals can influence the achievable density in confinement devices through several related mechanisms. While charge-exchange can increase the range over which neutral effects are important, penetration is significant only up to a line integral density of about  $10^{18} \text{ m}^{-2}$ , typically a small fraction of the plasma cross section. In this region, ionization and charge-exchange represent an energy transfer mechanism and may play a role similar to atomic radiation. It has been suggested, e.g. that thermal losses due to a density build-up near the X-point of a divertor plasma may trigger the H/L transition at high density [273]. Conversely, it has been suggested that energy carried by charge-exchange neutrals may stave off a radiative collapse by transporting heat from the plasma interior into the edge radiation zone [274]. In this model, the density limit arises when neutrals can no longer penetrate past the radiation zone. Neutrals may play an indirect role in the radiation balance through their effect on impurity generation. Recycling neutrals can dislodge atoms of wall material through physical or chemical sputtering processes [223]. Physical sputtering has an energy threshold below which the sputtering yields are negligible. Thus, the very high concentration of neutrals which occur near the density limit is unlikely to be an effective generator of impurities as the density is more than compensated by the lower temperatures. In addition, self-sputtering by impurity ions tends to dominate the physical sputtering source. Chemical sputtering rates are dependent mainly on the temperature of the wall material and thus can increase significantly at high neutral densities. This may be one of the reasons that higher densities are achievable only after carbon walls are coated with more inert materials.

The inability of neutrals to penetrate deeply into the plasmas may impose a fuelling limit on the plasma density. Over a wide range in temperature, the cross sections for ionization and charge-exchange are relatively constant; thus, the depth of penetration scales like  $1/n_e$ . This may give rise to a ‘soft’ density limit where ever increasing amounts of fuelling gas are required to reach a given plasma density. Thermal losses from the neutral interaction processes could cool the plasma periphery and enable radiation or transport mechanisms to take over and lead to a ‘hard’ or disruptive limit. The divertor/scrape-off model used to explain the density limit in JET discharges with beryllium walls found a fuelling limit which did not progress to a disruption due to the lack of strong radiation from higher  $Z$  materials [37, 227]. Unfortunately, little is known about the processes which take plasma ions up the density gradient into the plasma core. Without the knowledge of these mechanisms, it is not possible to predict the depth at which the plasma ionization source becomes ineffective. Calculations of these processes must also use self-consistent temperature profiles, requiring detailed knowledge of energy transport, which is not at hand. Still, there is evidence that limitations on fuelling rate may play an important practical role in determining achievable densities in large or high-field devices [233, 275]. Particle sources from neutral beams or pellets allow this limit to be circumvented and the similarity of the edge density limit for such plasmas, as compared to those fuelled by gas alone, suggests that fuelling itself is not responsible for the density limit described by  $n_G$ . It is important to note, however, that it is not possible, at this time, to predict the dynamics of edge fuelling processes for reactor scale devices where core fuelling will be less practical, if not impossible.

Finally, mechanisms have been proposed which rely on the neutral penetration depth to set the density and pressure gradient in the plasma edge [276, 268, 277]. This approach can be summarized in a straightforward, though highly simplified manner. Using curvature driven

modes with a maximum growth rate:

$$\gamma_{\max} \propto \sqrt{\frac{k_{\max} V_T^2}{R}} \propto \sqrt{\frac{V_T^2}{L_P R}} \quad (3.12)$$

These modes are stabilized by good curvature along the field lines at a rate

$$\omega_A \propto \frac{V_A}{qR} \quad (3.13)$$

where  $V_T$  is the ion thermal velocity,  $V_A$  is the Alfvén velocity and  $L_P$  is the pressure gradient length. Stability occurs for  $\gamma < \omega_A$ , thus

$$\frac{V_T^2}{V_A^2} = \beta_T < \frac{L_P}{q^2 R} \quad (3.14)$$

or rewriting,

$$\frac{nT}{L_P} < \frac{B_T^2}{q^2 R} = \frac{B_P^2 R}{a^2} \propto \frac{I_P^2 R}{a^4} \quad (3.15)$$

if  $L_P$  is set by neutral penetration and therefore proportional to  $1/n$ ; then

$$n < \frac{I_P}{a^2} \sqrt{\frac{R}{T}} \quad (3.16)$$

which is reasonably close to the experimental observations. Of course this derivation may be faulted on several grounds. Firstly, the stability calculation neglects the effects of the local magnetic shear, diamagnetic effects and so forth. Secondly, the balance of experimental evidence suggests that the edge gradient lengths are not set solely by neutral penetration.

#### 4. Summary

Understanding the density limit is crucial for projecting the performance of future machines. In recent years, a great deal of new data has been obtained and a better understanding of the physical processes involved has been achieved. Still, the basic mechanisms which set the value of the limit are uncertain. Unlike the operational limits for plasma pressure and current, which depend essentially on MHD physics alone, the density limit would seem to involve transport and atomic processes as well. The manifestation of the limit is configuration dependent. Tokamaks ultimately disrupt; RFP discharges may either end in ‘hard’ events, terminating rapidly, or as ‘soft’ gradual quenches; stellarators always manifest the limit as a soft quench. Before the disruptive limit, tokamaks exhibit a variety of phenomena. Thermal condensations (MARFES) may appear on the plasma midplane or near divertor plates; the divertor may detach, decoupling the plasma from the plates entirely; the entire discharge may detach from the wall poloidally, resting instead on a mantle of cooler, highly radiating gas. H-mode plasmas deteriorate progressively at high densities, with energy confinement degrading to a lesser or greater degree depending on plasma shape. The character of ELMs also changes, becoming smaller and more frequent as the limit is approached. Discharges always make a transition back to L-mode before reaching the disruptive limit. All of these are the result of edge cooling and provide a strong impetus to look for the physics of the tokamak density limit in the plasma edge. It is not certain that the limit in stellarators is also due to edge physics. There is evidence that it is caused by a more widespread imbalance between heating and loss power. The difference may be due to the difference in the way the two systems respond to local thermal collapse. In a stellarator, there is no plasma current to couple local temperature profiles to global stability.

Empirical scaling as embodied by the Greenwald limit provides a reasonable description of the operating space for tokamaks and RFPs. For the current generation of tokamaks operating with flat density profiles,  $n_G$  embodies the leading dependences and is accurate to about 10–20%. Similar agreement is seen in the RFP. The effects of shape are apparently well captured by the plasma current dependence. Strong shaping does allow for better H-mode confinement as the density is raised toward the limit. Power scaling is usually found to be weak, though some variation from machine to machine is apparent. The role of beam fuelling in the observed power dependence is unclear. Impurities are important insofar as very dirty plasmas cannot be operated at the highest densities. However, for  $Z_{\text{eff}}$  below 2–3, only small effects of the impurity levels are observed.

Stellarators reach higher densities than tokamaks with similar parameters, perhaps a factor of 2 or more when normalized to the Hugill's limit. The comparison should only be taken in a qualitative sense, since the density limit scalings are quite different in the two types of devices. Plasma current is apparently the important parameter for the tokamak rather than  $B/q_\phi$ , but stellarators have essentially no plasma current and their density limit does not seem to depend on the magnitude of the rotational transform. The size scaling for the limit in the two devices may be quite different as well; data from the new generation of very large stellarators will be helpful on this point. Density limits have not been clearly determined in the spheromak and FRC, but one can compare to their operation at 'optimized' densities. Typically the fill pressure is adjusted to allow creation of plasmas with the best stability and transport properties. The density for this optimum in operation agrees with the empirical scaling within a factor of about 2. It is not known whether this is a coincidence or the sign of some deeper mechanistic connection.

Global scaling can be important not only for its predictive power, but may serve as a guide toward a proper theory, the dominant parameters either pointing toward or away from particular physical mechanisms. For example, the experimental finding that the limit follows  $I/a^2$  more closely than  $B/qR$  [3, 72] might suggest that the dominant current scaling arises from the poloidal field rather than through a connection length. Similarly, from the lack of strong power scaling or dependence on impurity levels (for relatively clean plasmas) one may infer that cooling via atomic radiation is not a critical element in the process. The robustness of the limit, the observation that a simple law works for a wide variety of machine sizes and configurations, for limited and diverted machines, and for all first wall materials and geometry, suggests that the physical mechanism responsible should be robust as well. Global scaling does miss important local effects, in particular, the role of the density profile. The limit is apparently an edge phenomena, allowing additional particles to be added to the core with no deleterious effects as long as MHD modes are not destabilized by the peaked pressure profiles. Recent data from low aspect ratio tokamaks suggest that they are able to run above the empirical limit which was derived for standard aspect ratio machines. The role of density profiles in this effect is not yet clear.

While density limits have been observed for several decades, there is no widely accepted first-principles theory available. Two important questions must be answered; what causes the anomalous cooling? and at what density does that cooling lead to an operational limit? Motivated by the observation that radiation increases with density and that plasmas with high levels of impurities are unable to run at high densities, most work, to date, has concentrated on impurity radiation as the principal drive for the limit. To calculate the radiation driven limit, researchers have chosen one of the high-density phenomena, MARFES, poloidal detachment, or divertor detachment, and attempted to compute a density threshold for its onset or stability. Equations for energy, momentum, and particle conservation are solved either analytically or numerically with the density limit arising as a bifurcation or loss of solution. Cross-field

transport is an important ingredient in these calculations, with choices often guided by the need to match the empirical scaling. Typically the current or field scaling which is derived is due entirely to the transport model chosen. These assumptions do not necessarily match predictions from turbulence theory or experimental observations—a serious weakness in the models. In the absence of a reliable theory for particle transport, they must also make assumptions or use experimental data to translate the edge density threshold to a core density limit. These models are able to reproduce some features of experiments in some cases with good quantitative agreement. Size and safety factor dependence are due mainly to the parallel connection length. With some exceptions, these models predict moderately strong scaling with input power and impurity content, typically  $n_{\text{limit}} \propto \sqrt{P_{\text{in}}/(Z_{\text{eff}} - 1)}$  or something close to it, rather stronger than what is found in experiments. An alternate approach has been to solve the energy balance equation including the effects of neutral transport or radiation and to derive a limit by comparing the calculated pressure profile to MHD stability limits. These computations also require knowledge of cross-field particle and energy transport. Source terms should not be neglected; poor neutral penetration may make it difficult to reach the limit in many cases. However, this does not seem to be the physics behind the empirical limit and fuelling limits are routinely overcome in current experiments. At this point, it cannot be ascertained that this will be the case as the reactor regime is approached. It may be that fuelling limits set in before other physics limits. Options for fuelling in reactors are highly constrained by physics and economics.

There is evidence that increased transport at high densities is responsible for the edge cooling which is observed. Transient transport experiments have measured a systematic degradation in particle transport as the density is raised. These measurements are backed by observations of increased fluctuation levels. Detailed probe measurements in the edge plasma have found a regime of large scale fluctuations with long correlation times in the far scrape-off which grows inward toward the separatrix at high density. Near the density limit, this region extends past the separatrix, intruding into the core plasma. Parallel collisionality is apparently a critical parameter for this phenomenon. While these observations are consistent with the hypothesis of a transport driven density limit, edge transport theory is not sufficiently advanced to provide more than qualitative support. Current simulation work has discovered regimes of extremely large turbulent transport in parts of parameter space consistent with observations of the density limit. However, a comprehensive and well-characterized edge turbulence model will be needed before the hypothesis can be tested, let alone a predictive capability derived.

## 5. Discussion

The density limit manifests itself in discontinuous or catastrophic behaviour. The crucial questions that must be answered concern the physical processes which are essential for that behaviour. Experimental evidence suggests that mechanisms which lead to abnormally strong cooling in the edge plasma are responsible; however, no clear consensus on the details has emerged. Neither is it understood how simple scaling laws capture so much of the behaviour that is apparently due to the complicated physics involved. The basic similarity of the density limit across a wide variety of toroidal confinement schemes is remarkable. On the surface, this suggests a substantial degree of commonality for the physics and unification of the phenomenology. Elements of the underlying processes should contribute to this unification. The basic physics of atomic radiation is independent of machine configuration, though impurity sources do vary markedly depending on details of machine design and materials. Researchers have found essential similarities in edge turbulence across a wide range of confinement devices

[278]. Of course it is not impossible that this unification is misleading, the result of coincidence rather than deep symmetry.

Progress has been made in understanding many of the important underlying processes, but a widely applicable, first-principles predictive theory has not yet emerged. This should not be surprising as there is not even agreement on the essential mechanism. In all cases, the physics is complex and highly nonlinear; causes and effects are difficult to decouple. It is essential that self-consistent models for sources, sinks, transport, and profiles are used, suggesting a critical role for advanced simulations. At the least, analytical models will require substantial numerical backup. Of the two general types of models proposed, radiation and transport, neither is entirely satisfactory at the present time. Radiation theories depend on modelling particular phenomena which do not, in all cases, occur close to the density limit. Further, these models require knowledge of energy and particle transport for which a widely applicable theory is not available, making them, at best, incomplete. Transport based theories for the density limit are far less mature and are not able to make quantitative predictions at this point. The origin of the plasma current scaling is a significant challenge. Additional experiments are needed to determine if the anomalous transport behaviour reported in some devices is universal. The density limit may involve some mixture of atomic and transport physics. For example, destabilization of resistive gradient modes by radiation was proposed as an explanation for the enhanced edge transport seen near the density limit in MTX [246]. Both radiation and transport models have experimental ramifications which should be pursued. It is not clear that extensive work on a scalar database and global scaling would be particularly helpful in this regard. On the other hand, a multi-machine database of edge profiles could be useful and serve as the raw material for further model development.

### Acknowledgments

I would like to thank all of those who contributed their ideas and research to this review, particularly those who generously shared their figures. Any oversights or errors in interpretation are my own. This manuscript was prepared under support of US DOE grant DE-FC02-99ER54512.

### References

- [1] ITER Expert Groups 1999 *Nucl. Fusion* **39** 2137–74
- [2] Goldston R 1996 *Plasma Phys. Control. Fusion* **38** 1161–72
- [3] Greenwald M *et al* 1988 *Nucl. Fusion* **28** 2199–207
- [4] ITER Expert Groups 1999 *Nucl. Fusion* **39** 2175–250
- [5] Aymar R *et al* 2001 *Nucl. Fusion* **41** 1301–10
- [6] Stott P E *et al* 1978 *Proc. 8th European Conf. on Controlled Fusion and Plasma Physics (Prague, 1978)* vol 1 (ECA) p 37
- [7] Stabler A *et al* 1990 *Proc. 17th European Conf. on Controlled Fusion and Plasma Physics (Amsterdam, 1990)* vol 14B (part I) (ECA) pp 395–8
- [8] Stabler A *et al* 1993 *Proc. 9th International Conf. on Plasma Physics and Controlled Nuclear Fusion Research (Baltimore, 1992)* vol 2, pp 523–9
- [9] Stabler A *et al* 1992 *Nucl. Fusion* **32** 1557–83
- [10] Waidmann G and Guangli K 1992 *Nucl. Fusion* **32** 645–54
- [11] Andrejko M *et al* 1995 *Proc. 15th International Conf. on Plasma Physics and Controlled Nuclear Fusion Research (Seville, 1994)* vol 2, p 37
- [12] Pochelon A *et al* 1995 *Proc. 22nd European Physical Society Conf. on Controlled Fusion and Plasma Physics (Bournemouth, 1995)* vol 19C (part IV) (ECA) pp 81–4
- [13] Bartiromo R 2000 *Proc. 27th EPS Conf. on Controlled Fusion and Plasma Physics (Budapest, 2000)* vol 24B (ECA) pp 1380–3
- [14] Gao X *et al* 2000 *Phys. Plasmas* **7** 2933–8

- [15] Kaye S M *et al* 2000 *Phys. Plasmas* **8** 1977–87
- [16] Perkins F W *et al* 1997 *Proc. 16th International Atomic Energy Agency Conf. on Fusion Energy (Montreal, 1996)* vol 2, pp 963–9
- [17] Hosea J C, Bobeldijk C and Grove D J 1971 *Proc. 4th International Conf. Plasma Physics and Controlled Nuclear Fusion Research (Madison, 1970)* vol 2 (Vienna: IAEA) pp 415–40
- [18] Artsimovich L A 1972 *Nucl. Fusion* **12** 215–52
- [19] Vershkov V A and Mirnov S V 1974 *Nucl. Fusion* **14** 383–95
- [20] Murakami M, Callen J and Berry L 1976 *Nucl. Fusion* **16** 347–8
- [21] Paul J W M *et al* 1977 *Nucl. Fusion* **2** 269–85
- [22] Fielding S J *et al* 1977 *Nucl. Fusion* **17** 1382–5
- [23] Paul J W M 1979 *Proc. 9th European Conf. on Controlled Fusion and Plasma Physics (Oxford, 1979)* (ECA) pp 371–85
- [24] Axon K B *et al* 1981 *Proc. 8th International Conf. on Plasma Physics and Controlled Nuclear Fusion Research (Brussels, 1980)* vol 1 (Vienna: IAEA) pp 413–23
- [25] Hugill J *et al* 1983 High density operation in Dite with neutral beam injection *Culham Laboratory Report No CLM-R239*
- [26] Costa S *et al* 1982 *Nucl. Fusion* **22** 1301–11
- [27] Sykes A *et al* 2001 *Phys. Plasmas* **8** 2101–6
- [28] Hugill J 1983 *Nucl. Fusion* **23** 331–68
- [29] Scoville J T *et al* 1991 *Nucl. Fusion* **31** 875–90
- [30] Kaye S M *et al* 1997 *Nucl. Fusion* **37** 1303–28
- [31] Thomsen K *et al* 1999 *Proc. 17th International Conf. on Plasma Physics and Controlled Nuclear Fusion Research (Yokohama, 1998)* vol 3 (Vienna: IAEA) p 987
- [32] Saibene G *et al* 1999 *Nucl. Fusion* **39** 1133–56
- [33] Saibene G *et al* 1999 *Proc. 26th EPS Conf. on Controlled Fusion and Plasma Physics (Maastricht, 1999)* vol 23J (ECA) pp 97–100
- [34] LaBombard B 1986 Poloidal asymmetries in the limiter shadow plasma of the Alcator C tokamak *PhD Thesis MIT*
- [35] Erents S K *et al* 1989 *J. Nucl. Mater.* **162–164** 226–30
- [36] Hokin S A *et al* 1991 *Phys. Fluids* **3** 2241–6
- [37] Lowry C G *et al* 1990 *Proc. 17th European Conf. on Controlled Fusion and Plasma Physics (Amsterdam, 1990)* vol 14B (part I) (ECA) pp 339–42
- [38] Kamada Y *et al* 1991 *Nucl. Fusion* **31** 1827–33
- [39] Frigione D *et al* 1996 *Nucl. Fusion* **36** 1489
- [40] Stork D and JET Team 1997 *Proc. 16th International Atomic Energy Agency Fusion Energy Conf. (Montreal, 1996)* vol 1, p 189
- [41] Mertens V *et al* 1997 *Nucl. Fusion* **37** 1607
- [42] Zohm H 1996 *Plasma Phys. Control. Fusion* **38** 105–28
- [43] Niedermeyer H *et al* 1986 *Proc. 13th European Conf. on Controlled Fusion and Plasma Physics (Schliersee, 1986)* vol 10C (part 1) (ECA) pp 168–71
- [44] Greenwald M *et al* 1987 *Nucl. Fusion* **1** (suppl) **1** pp 139–49
- [45] Messiaen A *et al* 1996 *Phys. Rev. Lett.* **77** 2487–90
- [46] Maingi R *et al* 1998 *Proc. 17th IAEA Fusion Energy Conf. (Yokohama, 1998)* vol 2, p 793
- [47] Maingi R *et al* 1999 *J. Nucl. Mater.* **266** 598–603
- [48] Weynants R R *et al* 1999 *Nucl. Fusion* **39** 1637–48
- [49] Mahdavi M A *et al* 2000 *Proc. 18th IAEA Fusion Energy Conf. (Sorrento, 2000)* (Vienna: IAEA) p EXP1/04
- [50] Osborne T H *et al* 2001 *Phys. Plasmas* **8** 2017–22
- [51] Osborne T H *et al* 2001 *J. Nucl. Mater.* **290** 1013–17
- [52] Greenwald M *et al* 1995 *Phys. Plasmas* **2** 2308–13
- [53] Rapp J *et al* 1999 *Nucl. Fusion* **39** 765–76
- [54] LaBombard B *et al* 2001 *Phys. Plasmas* **8** 2107–17
- [55] Schuller P C *et al* 1984 *Proc. 12th European Conf. on Controlled Fusion and Plasma Physics (Budapest, 1984)* vol 9F (part I) (ECA) pp 151–4
- [56] Wesson J A *et al* 1985 *Proc. 12th European Conf. on Controlled Fusion and Plasma Physics (Budapest, 1985)* vol 9F (part I) (ECA) pp 147–50
- [57] Wesson J A *et al* 1989 *Nucl. Fusion* **29** 641–66
- [58] Campbell D *et al* 1994 *Proc. 21st EPS Conf. on Controlled Fusion and Plasma Physics (Montpellier, 1994)* vol 18B (part 1) (ECA) pp 2–5

- [59] Campbell D 1990 *Plasma Phys. Control. Fusion* **32** 949–64
- [60] Gruber O *et al* 1997 *Plasma Phys. Control. Fusion* **39** 9–13
- [61] Gorelik L *et al* 1972 *Nucl. Fusion* **12** 185–9
- [62] Alladio F *et al* 1982 *Phys. Lett.* **90A** 405
- [63] Baker D, Snider R T and Nagami M 1982 *Nucl. Fusion* **22** 807
- [64] Niedermeyer H *et al* 1983 *Proc. 11th European Conf. on Controlled Fusion and Plasma Physics (Aachen, 1983)* vol 7D (part II) (ECA) p 1128
- [65] Lipschultz B *et al* 1984 *Nucl. Fusion* **24** 977–88
- [66] Lipschultz B 1987 *J. Nucl. Mater.* **135–147** 15–25
- [67] McCracken G M *et al* 1987 *J. Nucl. Mater.* **145–147** 181–5
- [68] Mertens V *et al* 1997 *Proc. 16th International Conf. on Plasma Physics and Controlled Nuclear Fusion Research (Montreal, 1996)* vol 1 (Vienna: IAEA) pp 413–23
- [69] Lipschultz B *et al* 1998 *Phys. Rev. Lett.* **81** 1007–10
- [70] Asakura N *et al* 1999 *J. Nucl. Mater.* **206–209** 182
- [71] Hosogane N *et al* 1992 *J. Nucl. Mater.* **196** 750–4
- [72] Petrie T W, Kellman A G and Mahdavi M A 1993 *Nucl. Fusion* **33** 929–54
- [73] Mertens V *et al* 1994 *Plasma Phys. Control. Fusion* **36** 1307–25
- [74] Mertens V *et al* 1996 *Proc. 23rd EPS Conf. on Controlled Fusion and Plasma Physics (Kiev, 1996)* vol 20C (part 1) (ECA) pp 15–18
- [75] Shimomura Y *et al* 1983 *Nucl. Fusion* **23** 869–79
- [76] Allen S L *et al* 1995 *Plasma Phys. Control. Fusion* **37** A191–202
- [77] Lipschultz B *et al* 1995 *J. Nucl. Mater.* **220–222** 50–61
- [78] Matthews G F 1995 *J. Nucl. Mater.* **220–222** 104
- [79] Neuhauser J *et al* 1995 *Plasma Phys. Control. Fusion* **37** A37–51
- [80] Asakura N *et al* 1996 *Nucl. Fusion* **36** 795–813
- [81] Pitcher C S and Stangeby P C 1997 *Plasma Phys. Control. Fusion* **39** 779–930
- [82] LaBombard B *et al* 1995 *Phys. Plasmas* **2** 2242–8
- [83] Hutchinson I *et al* 1995 *Plasma Phys. Control. Fusion* **37** 1389
- [84] Borrass K, Lingertat J and Schneider R 1998 *Contributions to Plasma Physics (Berlin: Akademie)* vol 38 pp 1–2
- [85] Petrie T W *et al* 1997 *Nucl. Fusion* **37** 321–38
- [86] Petrie T W *et al* 1997 *J. Nucl. Mater.* **241–243** 639–44
- [87] Lipschultz B *et al* 1997 *Proc. 16th International Atomic Energy Agency Conf. on Fusion Energy (Montreal, 1996)* vol 1 (Vienna: IAEA) pp 425–36
- [88] Gruber O *et al* 1995 *Phys. Rev. Lett.* **74** 4217–20
- [89] Asakura N *et al* 1997 *Plasma Phys. Control. Fusion* **39** 1295–314
- [90] Saibene G *et al* 1997 *Proc. 24th EPS Conf. on Controlled Fusion and Plasma Physics (Berchtesgaden, 1997)* vol 21A (part I) (ECA) pp 49–52
- [91] Suttrop W *et al* 1999 *Plasma Phys. Control. Fusion* **41** A569–76
- [92] Mertens V *et al* 1998 *Proc. 25th EPS Conf. on Controlled Fusion and Plasma Physics (Prague, 1998)* vol 22C (part I) (ECA) pp 276–9
- [93] Ryter F *et al* 1998 *Plasma Phys. Control. Fusion* **40** 725–9
- [94] Kardaun O *et al* 1993 *Proc. 14th International Conf. on Plasma Physics and Controlled Fusion (Wurzburg, 1992)* vol 3 (Vienna: IAEA) pp 251–67
- [95] Ryter F *et al* 1996 *Plasma Phys. Control. Fusion* **38** 1279–82
- [96] Hubbard A *et al* 1997 *Proc. 16th International Atomic Energy Agency Conf. on Fusion Energy (Montreal, 1996)* vol 1 (Vienna: IAEA) pp 875–83
- [97] Greenwald M *et al* 1997 *Nucl. Fusion* **37** 793–807
- [98] Suttrop W *et al* 1997 *Plasma Phys. Control. Fusion* **39** 2051–66
- [99] Fukuda T *et al* 1998 *Plasma Phys. Control. Fusion* **40** 827–30
- [100] Hubbard A *et al* 1998 *Plasma Phys. Control. Fusion* **40** 689–92
- [101] Righi E *et al* 2000 *Plasma Phys. Control. Fusion* **42** A199–204
- [102] Osborne T H *et al* 2000 *Plasma Phys. Control. Fusion* **42** A175–84
- [103] Kamada Y *et al* 1997 *Proc. 16th International Conf. on Plasma Physics and Controlled Nuclear Fusion Research (Montreal, 1996)* vol 1 (Vienna: IAEA) pp 247–57
- [104] Budny R *et al* 2002 *Nucl. Fusion* **42** 66
- [105] Mertens V *et al* 2000 *Nucl. Fusion* **40** 1839–43
- [106] Stoiber J *et al* 2000 *Plasma Phys. Control. Fusion* **42** 27–9

- [107] Goetz J A *et al* 1999 *Phys. Plasmas* **6** 1899–906
- [108] Schuller F C 1995 *Plasma Phys. Control. Fusion* **37** A135–62
- [109] Sykes A and Wesson J A 1980 *Phys. Rev. Lett.* **44** 1215–18
- [110] Guzdar P N 1984 *Phys. Fluids* **27** 447–9
- [111] Yu G Y, Guzdar P N and Lee Y C 1985 *Nucl. Fusion* **25** 403–17
- [112] Dong J Q and Guzdar P N 1986 *Phys. Fluids* **29** 3090–3
- [113] Kleva R G 1989 *Comment. Plasma Phys. Control. Fusion* **13** 63–75
- [114] Bondeson A *et al* 1991 *Nucl. Fusion* **31** 1695–716
- [115] Kleva R G and Drake J F 1991 *Phys. Fluids B: Plasma Phys.* **3** 372–83
- [116] Hugill J 1979 *Proc. 9th European Conf. on Controlled Fusion and Plasma Physics (Oxford, 1979)* (ECA) p 151
- [117] JET 1987 *Proc. 11th International Conf. on Plasma Physics and Controlled Nuclear Fusion Research (Kyoto, 1986)* vol 1 (Vienna: IAEA) p 433
- [118] Alikae V V *et al* 1991 *Proc. 13th International Conf. on Plasma Physics and Controlled Nuclear Fusion Research (Washington, DC, 1990)* vol 1 (Vienna: IAEA) pp 163–76
- [119] Savrukhin P V *et al* 1994 *Nucl. Fusion* **34** 317–36
- [120] Suttrop W *et al* 1997 *Nucl. Fusion* **37** 119–25
- [121] Howard J and Persson M 1992 *Nucl. Fusion* **32** 361–77
- [122] ITER Expert Groups 1999 *Nucl. Fusion* **39** 2251–390
- [123] Vallet J C *et al* 1991 *Phys. Rev. Lett.* **67** 2662–8
- [124] Allen J *et al* 1986 *Plasma Phys. Control. Fusion* **28** 101–12
- [125] Strachan J *et al* 1987 *J. Nucl. Mater.* **145–147** 186–90
- [126] Parker R R *et al* 1989 *Proc. 12th International Conf. on Plasma Physics and Controlled Nuclear Fusion Research (Nice, 1988)* vol 2 (Vienna: IAEA) pp 341–56
- [127] Alladio F *et al* 1993 *Proc. 9th International Conf. on Plasma Physics and Controlled Nuclear Fusion Research (Baltimore, 1992)* vol 1, pp 141–51
- [128] Bell M G *et al* 1992 *Nucl. Fusion* **32** 1585–91
- [129] Sykes A *et al* 1995 *Proc. 15th International Conf. on Plasma Physics and Controlled Nuclear Fusion Research (Seville, 1994)* vol 1 (Vienna: IAEA) pp 719–24
- [130] Sykes A *et al* 1997 *Plasma Phys. Control. Fusion* **39** B247–60
- [131] Greenwald M *et al* 1984 *Phys. Rev. Lett.* **53** 352
- [132] Messiaen A M *et al* 1994 *Nucl. Fusion* **34** 825–36
- [133] Milora S *et al* 1995 *Nucl. Fusion* **33** 657–754
- [134] Koide Y *et al* 1996 *Plasma Phys. Control. Fusion* **38** 1011–22
- [135] Burrell K H 1997 *Phys. Plasmas* **4** 1499–518
- [136] Synakowski E J *et al* 1997 *Phys. Plasmas* **4** 1736–44
- [137] Sips A C C *et al* 1998 *Plasma Phys. Control. Fusion* **40** 1171–84
- [138] Stabler A *et al* 1989 *Proc. 16th European Conf. on Controlled Fusion and Plasma Physics (Venice, 1989)* vol 13B (part I) (ECA) pp 23–6
- [139] Aikawa H *et al* 1989 *Proc. 12th International Conf. on Plasma Physics and Controlled Nuclear Fusion Research (Nice, 1988)* vol 1 (Vienna: IAEA) pp 67–81
- [140] Kamada Y *et al* 1990 Density limit in JT-60 Japan Atomic Energy Res. Inst. Report No 90-081
- [141] Lang P T *et al* 1995 *Proc. 22nd EPS Conf. on Controlled Fusion and Plasma Physics (Bournemouth, 1995)* vol 19C (part 2) (ECA) pp 449–51
- [142] Lang P *et al* 1996 *Nucl. Fusion* **36** 1531–45
- [143] Mahdavi M A *et al* 1997 *Proc. 24th EPS Conf. on Controlled Fusion and Plasma Physics (Berchtesgaden, 1997)* vol 21A (part III) (ECA) p 1113
- [144] Maingi R *et al* 1997 *Phys. Plasmas* **4** 1752–60
- [145] Engelhardt W *et al* 1979 *Proc. 7th International Conf. on Plasma Physics and Controlled Nuclear Fusion Research (Innsbruck, 1978)* vol 1 (Vienna: IAEA) pp 123–34
- [146] Soldner F X *et al* 1988 *Phys. Rev. Lett.* **61** 1105–8
- [147] Fiore C L *et al* 2001 *Phys. Plasmas* **8** 2023–8
- [148] McKee G R *et al* 2000 *Phys. Plasmas* **7** 1870–7
- [149] Biglari H, Diamond P H and Terry P W 1990 *Phys. Fluids B: Plasma Phys.* **2** 1–4
- [150] Messiaen A M *et al* 1997 *Phys. Plasmas* **4** 1690–8
- [151] Unterberg B *et al* 1997 *Plasma Phys. Control. Fusion* **39** 9–13
- [152] Ongena J *et al* 1999 *Plasma Phys. Control. Fusion* **41** A379–99
- [153] Mank G *et al* 2000 *Phys. Rev. Lett.* **85** 2312–15

- [154] Ongena J *et al* 2000 *Phys. Plasmas* **8** 2188–98
- [155] Rapp J *et al* 1998 *Proc. 17th IAEA Fusion Energy Conf. (Yokohama, 1998)* vol 2 (Vienna: IAEA) pp 781–4
- [156] Chankin A V 1997 *Plasma Phys. Control. Fusion* **39** 1059–82
- [157] Stober J *et al* 2001 *Nucl. Fusion* **41** 1123–34
- [158] Matthews G F *et al* 1999 *J. Nucl. Mater.* **266** 1134–8
- [159] Axon K B *et al* 1979 *Proc. 7th International Conf. on Plasma Physics and Controlled Nuclear Fusion Research (Innsbruck, 1978)* vol 1 (Vienna: IAEA) pp 51–64
- [160] Nieswand C *et al* 1995 *Czech. J. Phys.* **45** 1095
- [161] Lazarus E *et al* 1984 *J. Nucl. Mater.* **121** 61–8
- [162] Lazarus E *et al* 1985 *Nucl. Fusion* **25** 135–49
- [163] Ongena J and Messiaen A M 1993 *Proc. 20th European Conf. on Controlled Fusion and Plasma Physics (Lisbon, 1993)* vol 17C (part I) (ECA) pp 127–30
- [164] Greenwald M *et al* 1985 *Proc. 10th International Conf. on Plasma Physics and Controlled Nuclear Fusion Research (London, 1984)* vol 1 (Vienna: IAEA) pp 45–55
- [165] McKee G *et al* 2000 *Phys. Rev. Lett.* **84** 1922–5
- [166] Samm U *et al* 1989 *Proc. 16th Conf. on Controlled Fusion and Plasma Physics (Venice, 1989)* (part III) (ECA) pp 995–8
- [167] Horton L 1998 *Proc. 25th EPS Conf. on Controlled Fusion and Plasma Physics (Prague, 1998)* vol 22C (part I) (ECA) p 30
- [168] Duesing G 1986 *Plasma Phys. Control. Fusion* **28** 1429–34
- [169] Umansky M V *et al* 1998 *Phys. Plasmas* **5** 3373–6
- [170] Horton L D 1997 *Proc. 24th EPS Conf. on Controlled Fusion and Plasma Physics (Berchtesgaden, 1997)* vol 21A (part I) (ECA) pp 65–8
- [171] Schmidt G L, Milora S and Arunsalem V 1987 *Proc. 11th International Conf. on Plasma Physics and Controlled Nuclear Fusion Research (Kyoto, 1986)* vol 1 (Vienna: IAEA) p 171
- [172] JET 1987 *Plasma Phys. Control. Fusion* **29** 1219
- [173] Bickerton R 1987 *Plasma Phys. Control. Fusion* **29** 1219–33
- [174] Antoni V *et al* 1983 *Proc. 9th International Conf. on Plasma Physics and Controlled Nuclear Fusion Research (Baltimore, 1982)* vol 1, pp 619–40
- [175] Ortolani S 1988 *Proc. Course and Workshop on the Physics of Mirrors, Reversed Field Pinches and Compact Tori (Varenna 1988)* vol 1 (Bologna: Editrice Compositori) pp 107–44
- [176] Buffa A *et al* 1981 *Proc. 8th International Conf. on Plasma Physics and Controlled Nuclear Fusion Research (Brussels, 1980)* vol 2 (Vienna: IAEA) pp 275–88
- [177] Perkins F W and Hulse R A 1985 *Phys. Fluids* **28** 1837–44
- [178] Bodin H A B *et al* 1983 *Proc. 9th International Conf. on Plasma Physics and Controlled Nuclear Fusion Research (Baltimore, 1982)* vol 1, pp 641–57
- [179] Tamano T *et al* 1983 *Proc. 9th International Conf. on Plasma Physics and Controlled Nuclear Fusion Research (Baltimore, 1982)* vol 1, pp 609–18
- [180] Baker D *et al* 1983 *Proc. 9th International Conf. on Plasma Physics and Controlled Nuclear Fusion Research (Baltimore, 1982)* vol 1, pp 587–95
- [181] Hokin S A *et al* 1993 *J. Fusion Energy* **12** 281–7
- [182] Robinson D C and King R E 1969 *Proc. 3rd International Conf. on Plasma Physics and Controlled Nuclear Fusion (Novosibirsk, 1968)* vol 1 (Vienna: IAEA) pp 263–75
- [183] Ogawa K *et al* 1983 *Proc. 9th International Conf. on Plasma Physics and Controlled Nuclear Fusion Research (Baltimore, 1982)* vol 1, pp 575–85
- [184] Antoni V *et al* 1983 *Proc. 11th European Conf. on Controlled Fusion and Plasma Physics (Aachen, 1983)* vol 7D (part I) (ECA) pp 143–6
- [185] Antoni V *et al* 1985 *Proc. 10th International Conf. on Plasma Physics and Controlled Nuclear Fusion (London, 1984)* vol 2 (Vienna: IAEA) pp 487–99
- [186] Marrelli L *et al* 1998 *Nucl. Fusion* **38** 649–59
- [187] Bolzonella T *et al* 1999 *Proc. 26th EPS Conf. on Controlled Fusion and Plasma Physics (Maastricht, 1999)* vol 23J (ECA) pp 1169–72
- [188] Wagner F 1997 *Plasma Phys. Control. Fusion* **39** 23–50
- [189] Wootton A J, Tsui H Y W and Prager S 1992 *Plasma Phys. Control. Fusion* **34** 2023–30
- [190] Sudo S *et al* 1990 *Nucl. Fusion* **30** 11–22
- [191] Giannone L *et al* 2000 *Plasma Phys. Control. Fusion* **42** 603–27
- [192] Atkinson D W *et al* 1981 *Proc. 8th International Conf. on Plasma Physics and Controlled Nuclear Fusion Research (Brussels, 1980)* vol 1 (Vienna: IAEA) pp 161–9

- [193] Grigull P *et al* 2001 *Plasma Phys. Control. Fusion* **43** A175–93
- [194] Sudo S *et al* 1985 *Nucl. Fusion* **25** 94–9
- [195] Lyon J *et al* 1997 Stellarator power plant study—stellarator physics *UC San Diego Report* No UCSD-ENG-004
- [196] Itoh K and Itoh S I J 1988 *J. Phys. Soc. Japan* **57** 1269–72
- [197] Barnes C *et al* 1985 *Proc. 7th Symp. Physics and Technology of Compact Toroids in the Magnetic Fusion Energy Program (Santa Fe, 1985)* (LANL) p 44
- [198] Henins I *et al* 1985 *Proc. 7th Symp. Physics and Technology of Compact Toroids in the Magnetic Fusion Energy Program (Santa Fe, 1985)* (LANL) p 63
- [199] Jarboe T 1985 *Proc. 7th Symp. Physics and Technology of Compact Toroids in the Magnetic Fusion Energy Program (Santa Fe, 1985)* (LANL) pp 34–8
- [200] Jarboe T *et al* 1984 *Phys. Fluids* **27** 13–18
- [201] Wright B L *et al* 1985 *Nucl. Fusion* **25** 1313
- [202] Kato Y *et al* 1987 *Proc. Course and Workshop on the Physics of Mirrors, Reversed Field Pinches and Compact Tori (Varenna, 1987)* vol 3 (Bologna: Editrice Compositori SIF) pp 1137–43
- [203] Janos A 1987 *Proc. Course and Workshop on the Physics of Mirrors, Reversed Field Pinches and Compact Tori (Varenna, 1987)* vol 2 (Bologna: Editrice Compositori SIF) pp 595–615
- [204] Wang Z *et al* 2001 *Rev. Sci. Instrum.* **72** 1059–62
- [205] McKenna K F *et al* 1985 *Nucl. Fusion* **25** 1317
- [206] Tuszewski M *et al* 1991 *Phys. Fluids B: Plasma Phys.* **3** 2844–55
- [207] Ohkuma Y *et al* 1998 *Nucl. Fusion* **38** 1501–9
- [208] Okada S *et al* 2001 *Nucl. Fusion* **41** 625–9
- [209] Itoh K, Itoh S I and Giannone L 2000 Modelling density limit phenomena in toroidal helical plasmas *NIFS Report* No 627
- [210] Wobig H 2000 *Plasma Phys. Control. Fusion* **42** 931–48
- [211] Furth H 1970 *Phys. Fluids* **13** 3020
- [212] Gibson A 1976 *Nucl. Fusion* **16** 546–50
- [213] Rebut P H and Green B J 1976 *Nucl. Fusion* **2** (suppl) pp 3–16
- [214] Ohyabu N 1979 *Nucl. Fusion* **19** 1491–7
- [215] Ashby D E T F and Hughes M H 1981 *Nucl. Fusion* **21** 911–26
- [216] Roberts D E 1983 *Nucl. Fusion* **23** 311–29
- [217] Lipschultz B 1989 *Proc. Satellite Workshop of the 9th International Conf. on Plasma Surface Interactions (Cadarache, 1989)* (Saint-Paul-Lez-Durance: EUR-CEA) p 97
- [218] Connor J W and You S 2002 *Plasma Phys. Control. Fusion* **44** 121
- [219] Neuhauser J, Schneider W and Wunderlich R 1985 *Proc. 12th European Conf. on Controlled Fusion and Plasma Physics (Budapest, 1985)* vol 9F (part II) (ECA) pp 476–9
- [220] Stringer T E 1985 *Proc. 12th European Conf. on Controlled Fusion and Plasma Physics (Budapest, 1985)* vol 9F (part I) (ECA) pp 86–9
- [221] Drake J F 1987 *Phys. Fluids* **30** 2429
- [222] Tokar M Z 1989 *Proc. 16th European Conf. on Controlled Fusion and Plasma Physics (Venice, 1989)* vol 13B (part III) (ECA) pp 1035–8
- [223] Stangeby P C 2000 *The Plasma Boundary of Magnetic Fusion Devices* (Bristol: Institute of Physics)
- [224] Wesson J A and Hender T C 1993 *Nucl. Fusion* **33** 1019–24
- [225] De Ploey A, Van der Linden R A M, Huysmans G T A, Goossens M, Kerner W and Goedbloed J P 1997 *Plasma Phys. Control. Fusion* **39** 423–38
- [226] Borrass K 1991 *Nucl. Fusion* **31** 1035–51
- [227] Borrass K *et al* 1993 *Nucl. Fusion* **33** 63–76
- [228] Guzdar P N, Liu C S and Dong J Q 1988 *Nucl. Fusion* **28** 1791–9
- [229] Tokar M 1994 *Plasma Phys. Control. Fusion* **36** 1819–43
- [230] Stacey W M 1997 *Phys. Plasmas* **4** 1069–79
- [231] Wesson J A 1997 *Tokamaks* 2nd edn (Oxford: Oxford Science Publications)
- [232] Tokar M 2000 *Phys. Plasmas* **7** 2432–8
- [233] Stacey W M 1998 *Phys. Plasmas* **5** 3656–68
- [234] Neuhauser J and Wunderlich R 1987 *J. Nucl. Mater.* **145–147** 877–80
- [235] Capes H *et al* 1990 *Plasma Phys. Control. Fusion* **32** 103–13
- [236] Borrass K, Schneider R and Farengo R 1997 *Nucl. Fusion* **37** 523–37
- [237] Coster D P, Borrass K and Schneider R 1999 *J. Nucl. Mater.* **266** 804–8
- [238] Horton L 2000 *Plasma Phys. Control. Fusion* **42** A37–49
- [239] Lipschultz B *et al* 1997 *J. Nucl. Mater.* **241–243** 771–76

- [240] LaBombard B *et al* 1997 *J. Nucl. Mater.* **241–243** 149–66
- [241] Erents S K and Stangeby P C 1998 *Nucl. Fusion* **38** 1637–50
- [242] Giannone L *et al* 1997 *Proc. 24th EPS Conf. on Controlled Fusion and Plasma Physics (Berchtesgaden, 1997)* (part IV) (ECA) pp 1565–8
- [243] Giannone L *et al* 1999 *J. Nucl. Mater.* **266** 507–12
- [244] Allen J *et al* 1987 *Nucl. Fusion* **1** (suppl) 227–35
- [245] Suttrop W *et al* 1999 *J. Nucl. Mater.* **266–269** 118–23
- [246] Marinak M M 1995 *Nucl. Fusion* **35** 399–408
- [247] Brower D L *et al* 1991 *Phys. Rev. Lett.* **67** 200–3
- [248] Rowan W L *et al* 1995 *J. Nucl. Mater.* **220–222** 668–71
- [249] Junker W 1995 Investigations of the influence of thermal instabilities on the density limit in tokamaks  
*PhD Thesis* Max-Planck-Inst. Plasmaphys, Garching, Germany
- [250] Vershkov V A *et al* 1997 *J. Nucl. Mater.* **241–243** 873–7
- [251] Watkins J *et al* 1995 *J. Nucl. Mater.* **220–222** 347–51
- [252] Asakura N *et al* 1997 *J. Nucl. Mater.* **241–243** 559–63
- [253] Sardei F *et al* 1995 *J. Nucl. Mater.* **220–222** 736–40
- [254] Feng Y *et al* 1999 *J. Nucl. Mater.* **266–269** 928–33
- [255] Moyer R *et al* 1997 *J. Nucl. Mater.* **241–243** 633–8
- [256] Endler M 1995 *Nucl. Fusion* **35** 1307
- [257] Harvey R and Dendy R O 1992 *Phys. Fluids B: Plasma Phys.* **4** 902–10
- [258] Thayer D and Diamond P 1987 *Phys. Fluids* **30** 3724–34
- [259] Dnestrovskii A Y, Ivanov V V and Parail V 1988 *Sov. J. Plasma Phys.* **14** 529–33
- [260] Dnestrovskii A Y *et al* 1991 *Proc. 13th International Conf. on Plasma Physics and Controlled Nuclear Fusion Research (Washington, 1990)* vol 2 (Vienna: IAEA) pp 393–401
- [261] Guzdar P N *et al* 1993 *Phys. Fluids B: Plasma Phys.* **5** 3712–27
- [262] Rogers B N and Drake J F 1997 *Phys. Rev. Lett.* **79** 229–32
- [263] Scott B D 1997 *Plasma Phys. Control. Fusion* **39** 471–504
- [264] Scott B D 1997 *Plasma Phys. Control. Fusion* **39** 1635
- [265] Rogers B N and Drake J F 1998 *Proc. 17th IAEA Fusion Energy Conf. (Yokohama, 1998)* vol 4 (Vienna: IAEA) pp 1505–11
- [266] Rogers B N, Drake J F and Zeiler A 1998 *Phys. Rev. Lett.* **81** 4396–9
- [267] Diamond P 2001 Personal communication
- [268] Strauss H R 1983 *Phys. Fluids* **26** 2219–21
- [269] Krasheninnikov S I 2001 *Phys. Lett. A* **283** 368–70
- [270] Hass F and Thyagaraja A 1986 *Plasma Phys. Control. Fusion* **28** 1093–123
- [271] Hass F and Thyagaraja A 1992 *Phys. Rev. Lett.* **68** 891
- [272] Chankin A V and Saibene G 1999 *Plasma Phys. Control. Fusion* **41** 913–30
- [273] Petrie T W *et al* 1999 *J. Nucl. Mater.* **266–269** 642–7
- [274] Tokar M Z 1983 *Nucl. Fusion* **23** 1395–8
- [275] Vlases G C *et al* 1999 *J. Nucl. Mater.* **266** 160–7
- [276] Lehnert B 1975 *Nucl. Fusion* **15** 793–8
- [277] Tendler M 1984 *Nucl. Fusion* **24** 937–40
- [278] Sanchez E *et al* 2000 *Phys. Plasmas* **7** 1408–16